



Aristotle University of Thessaloniki

Faculty of Sciences
Department of Physics

Bachelor Thesis

Author:

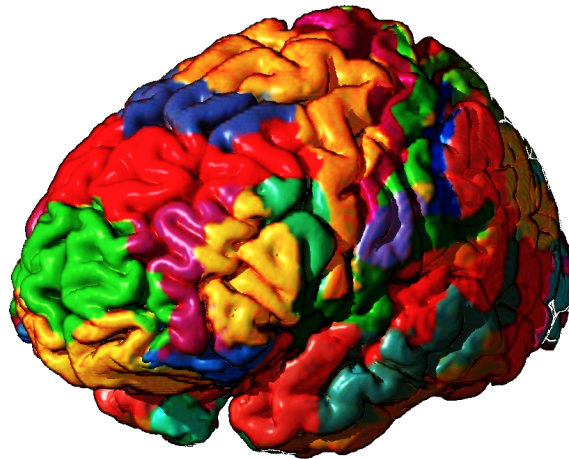
Kasapakis Nikolaos¹

Supervisor:

Prof. Theodoros Samaras²

Decoding and Classification of Category-Specific Visual Stimuli in the Fusiform Gyrus Using fMRI Data and Machine Learning

September 2, 2024



¹nkasapak@auth.gr, <https://github.com/kasapakis-nk>

²theosama@auth.gr, <https://www.physics.auth.gr/people/129>

³This thesis is licensed under the [Creative Commons Attribution-ShareAlike 4.0 Int. License \(CC BY-SA 4.0\)](https://creativecommons.org/licenses/by-sa/4.0/).

This page intentionally left blank.

Abstract

Decoding and Classification of Category-Specific Visual Stimuli in the Fusiform Gyrus Area Using fMRI Data and Machine Learning

Kasapakis Nikolaos

This thesis examines the use of Functional Magnetic Resonance Imaging (fMRI) data from the Human Connectome Project (HCP) to analyze neural systems involved in the processing of category-specific visual stimuli. It focuses on the Working Memory (WM) task within a broad fMRI paradigm designed to explore various neural domains including visual, language, and decision-making systems. Specifically, the study examines brain activation patterns in the Fusiform Face Area (FFA) related to different stimulus categories such as faces, places, tools, and body parts. Employing a pipeline of preprocessing steps followed by Multi-Variate Pattern Analysis (MVPA), the research assesses distributed patterns of voxel activation allowing for complex and detailed analyses of cognitive states. Data is processed through a Support Vector Machine (SVM) classification script developed for this study, aiming to differentiate between faces and other stimulus categories based solely on fMRI data. The thesis also addresses classification methodologies, with a particular focus on optimizing classifier accuracy by adjusting parameters like the number of data chunks, fold counts for cross-validation, and subject counts. The findings offer insights into the distinct brain activation patterns associated with different stimuli in the Fusiform Gyrus, contributing to our understanding of neural mechanisms in cognitive processes and practical applications for these insights.

This page intentionally left blank.

Περίληψη

Αποκωδικοποίηση και Κατηγοριοποίηση Κατηγορικών Οπτικών Ερεθισμάτων στην Ατρακτοειδή Έλικά με Χρήση Δεδομένων fMRI και Μηχανικής Μάθησης

Κασαπάκης Νικόλαος

Αυτή η εργασία εξετάζει τη χρήση δεδομένων λειτουργικής μαγνητικής τομογραφίας (fMRI) από το HCP για την ανάλυση των νευρωνικών συστημάτων που εμπλέκονται στην επεξεργασία κατηγορικών οπτικών ερεθισμάτων. Επικεντρώνεται στη δοκιμασία Λειτουργικής Μνήμης (WM) μέσα σε ένα ευρύτερο πείραμα fMRI που έχει σχεδιαστεί για να εξερευνήσει διάφορους νευρωνικούς τομείς, συμπεριλαμβανομένων των συστημάτων όρασης, γλώσσας και λήψης αποφάσεων. Συγκεκριμένα, η μελέτη εξετάζει τα μοτίβα ενεργοποίησης του εγκεφάλου στην περιοχή της Ατρακτοειδούς Έλικας που σχετίζονται με διάφορες κατηγορίες οπτικών ερεθισμάτων, όπως πρόσωπα, τοποθεσίες, εργαλεία και μέρη του σώματος. Χρησιμοποιώντας μια σειρά προεπεξεργαστικών βημάτων ακολουθούμενη από Ανάλυση Πολυδιάστατων Μοτίβων (MVPA), η έρευνα αξιολογεί καταναμεμημένα μοτίβα ενεργοποίησης, επιτρέποντας σύνθετες και λεπτομερείς αναλύσεις των γνωστικών καταστάσεων. Τα δεδομένα επεξεργάζονται μέσω ενός υπολογιστικού προγράμματος κατηγοριοποίησης SVM που αναπτύχθηκε για αυτή τη μελέτη, με στόχο τη διάκριση μεταξύ προσώπων και άλλων κατηγοριών ερεθισμάτων βασιζόμενων αποκλειστικά σε δεδομένα fMRI. Η εργασία εξετάζει επίσης μεθοδολογίες ταξινόμησης, δίνοντας ιδιαίτερη έμφαση στη βελτιστοποίηση της ακρίβειας του κατηγοριοποιητή με την προσαρμογή παραμέτρων όπως ο αριθμός των ανεξάρτητων τμημάτων δεδομένων, ο αριθμός επαναληπτικών διασταυρώσεων για επικύρωση και ο αριθμός των υποκειμένων των οποίων τα δεδομένα εμπλέκονται. Τα ευρήματα προσφέρουν πληροφορίες για τα διακριτά μοτίβα ενεργοποίησης του εγκεφάλου που σχετίζονται με διάφορα ερεθίσματα στην Ατρακτοειδή Έλικά, συμβάλλοντας στην κατανόησή μας για τους νευρωνικούς μηχανισμούς στις γνωστικές διαδικασίες και στην ανάπτυξη πιθανών πρακτικών εφαρμογών μέσω αυτών των ευρημάτων.

This page intentionally left blank.

Acknowledgements

First and foremost, I would like to express my deepest gratitude to Prof. Theodoros Samaras for his support and guidance throughout every stage of this work. I am equally indebted to Dimitris Stoupis, (titles:PhD ABD), whose expertise in academic matters, neuroscience, neuroanatomy, coding and statistics was instrumental in navigating the complexities of this research. His constant assistance and acumen were crucial to the successful completion of this project.

Beyond the technical work and analysis, the review process is crucial to ensuring the highest quality outcome. For this, I am profoundly grateful to my significant other, Ioanna-Anastasia Koukouli, for her unwavering support and encouragement throughout this journey. Her key insights into the design of this thesis were instrumental in shaping the final work, and her thoughtful input greatly enriched the overall direction of the project.

In any research endeavor, there are often unsung heroes who play a vital role behind the scenes. I believe it is essential to acknowledge them here. The open knowledge and open-source communities deserve special recognition for their immediate and high-quality support, whether through forums or mailing lists. Their collective wisdom greatly aided in resolving various technical challenges. I hope all contributors have been given the deserved credit.

This page intentionally left blank.

Contents

1	Theoretical Background	1
1.1	Introduction	1
1.2	Visual Information Flow In The Brain	1
1.2.1	The Optic Pathway	1
1.2.2	Information Processing In The Visual Cortex	2
1.2.3	Category-Specific Information Processing Areas In The Extrastriate Visual Cortex	3
1.3	Mechanisms of Functional Magnetic Resonance Imaging	4
1.3.1	Fundamentals of NMR Signal Generation	4
1.3.2	Relaxation Time Constants	5
1.3.3	Blood Oxygen Level Dependent (<i>BOLD</i>) Signal	7
2	Data Acquisition and Manipulation	11
2.1	The Human Connectome Project (<i>HCP</i>)	11
2.1.1	Task-fMRI Battery of the HCP	12
2.1.2	Working Memory Task of the HCP	13
2.2	Analysis of fMRI Signal	14
2.2.1	Univariate Pattern Analysis	14
2.2.2	Multivariate Pattern Analysis (<i>MVPA</i>)	15
2.2.3	Data Processing, Model Fitting and Classification	16
3	Methods	19
3.1	Pipeline Overview	19
3.2	Pipeline Segments	19
3.2.1	Preprocessing	19
3.2.2	Statistical Analysis	20
3.2.3	Dataset Extraction - Construcion	21
3.2.4	Mask Creation - Application	21
3.2.5	Partitioning of Masked Dataset	21
3.2.6	Classifier Training and Testing (<i>MVPA</i>)	22
3.3	Data Analysis	22
3.3.1	Category-Secific Baseline Brain Activation (<i>UPA</i>)	22
3.3.2	Classifier Performance - Chunks per Subject	23
3.3.3	Detecting Outlier Subjects	23
3.3.4	Classifier Performance - Fold Count	23
3.3.5	Classifier Performance - Subject Count	24
3.3.6	Ideal Parameters Performance	24
4	Classification Results & Discussion	25
4.1	Category-Secific Baseline Brain Activation (<i>UPA</i>) - Results	25
4.2	Fusiform Face Area <i>MVPA</i> - Results	26
4.2.1	Chunks Per Subject (<i>FFA</i>) - Results	26
4.2.2	Outlier Subjects (<i>FFA</i>) - Results	26
4.2.3	Fold Count (<i>FFA</i>) - Results	27
4.2.4	Subject Count (<i>FFA</i>) - Results	28

4.3	Parahippocampal Place Area MVPA - Results	29
4.3.1	Chunks per Subject (<i>PPA</i>) - Results	29
4.3.2	Outlier Subjects (<i>PPA</i>) - Results	29
4.3.3	Fold Count (<i>PPA</i>) - Results	30
4.3.4	Subject Count (<i>PPA</i>) - Results	30
4.4	Classification Ideal Parameters	31
4.4.1	Classifier Maximum Accuracy - Results	31
4.4.2	Classifier Maximum Efficiency - Results	31
4.4.3	Classifier Maximum Practicality - Results	32
5	Conclusions	33
	Glossary	35
	Acronyms	37
	Bibliography	39

List of Figures

1.1	The Visual Pathway	2
1.2	Visual Information Flow Bifurcation	2
1.3	Brain Regions of Interest	4
1.4	T1 Relaxation	5
1.5	T2 Relaxation	6
1.6	NMR Signal	7
1.7	Oxy- and Deoxy-hemoglobin Magnetic Moment Density	8
1.8	Stimulus-evoked response in somatosensory cortex of rats	8
2.1	HCP Image Acquisition Schematic Summary	12
2.2	Illustration of the difference between MVPA and UPA	15
2.3	Unprocessed Time-Series	16
2.4	Preprocessed Time-Series	16
2.5	Fundamental HRF Shapes	17
2.6	Fitted Time-Series	17
3.1	Pipeline Overview	19
3.2	Illustration of FFA and PPA masks	21
3.3	Illustration of Supervised Learning Classification	22
4.1	Activation Magnitude Per Stimulus Category (<i>UPA</i>) Bar Plots for the FFA	25
4.2	Activation Magnitude Per Stimulus Category (<i>UPA</i>) Bar Plots for the FFA Centrally	25
4.3	Activation Magnitude Per Stimulus Category (<i>UPA</i>) Bar Plots for the PPA	26
4.4	Individual Subjects' Accuracies Boxplots for the FFA	27
4.5	Accuracies Across 3000 Folds Boxplots For The FFA	27
4.6	Accuracies At Optimal Fold Count Boxplots For The FFA	28
4.7	Accuracies Across Subject Counts For The FFA	28
4.8	Individual Subjects' Accuracies Boxplots for the PPA	29
4.9	Accuracies Across 3000 Folds Boxplots For The PPA	30
4.10	Accuracies At Optimal Fold Count Boxplots For The PPA	30
4.11	Accuracies Across Subject Counts For The PPA	31

This page intentionally left blank.

List of Tables

2.1	HCP WM Task Event Sequence	13
3.1	Analysis Subject IDs	19
3.2	2C Analyses COPEs	20
3.3	4C Analyses COPEs	20

This page intentionally left blank.

Chapter 1

Theoretical Background

1.1 Introduction

The significance of the sense of vision for humans, in our contemporary everyday lives as well as in our evolution as a species, cannot be understated. While there is no clear consensus that vision is our most important sense, since that is dependent on one's cultural, societal and technological influences, there exists a large body of data drawn from cross-sectional observational research and surveys, as well as expert opinion of practitioners and researchers that leans towards the fact that vision is considered the most valued sense to the public.

Since prehistoric times, it is our vision that has aided us in our survival, by means of allowing us to advantageously select healthy mates, forage ripe fruit against a green foliage and detect predators through their natural camouflage, just to name a few benefits. Even in today's world, the majority of the information we process hails from our eyesight, whether it originates from the environment or from a computer screen.

However controversial the topic of the superiority of vision over our other senses might be, what is truly undebatable is that our evolution and eventual dominance as a species has been a consequence of the capabilities of our brain. It is the current form of the human brain after all, displaying an astonishingly intricate way in which it processes visual stimuli, that was preferentially chosen through natural selection to translate visual information to fit the species' best interests. Thus, it could be argued that to achieve a holistic understanding of the sense of vision, we need to delve into the patterns of activation induced in the brain by visual stimulation.

1.2 Visual Information Flow In The Brain

Light entering the eye creates a cascade of neuronal events throughout the optic pathway, which describes the anatomical pathway by which electrical signals generated by the retina are sent to the brain.

1.2.1 The Optic Pathway

The optic pathway begins in the retina, which is a complex structure made up of ten different layers. Notably, the photoreceptor layers consist of the rods and cones, which generate action potentials with the help of rhodopsin through photosensitive cycles. The ganglion cell layer and nerve fiber layer serve as the foundation of the optic nerve; the former contains the cell bodies, and the latter contains the axons as they stream across the retina. The nerve is surrounded by the dura, which is a continuation of that of the brain, allowing free movement of Cerebrospinal Fluid (CSF) between the eye and the intracranial vault. The axons exit the orbital part of the optic nerve through the orbital foramen, simultaneously with the ophthalmic artery and sympathetic fibers.

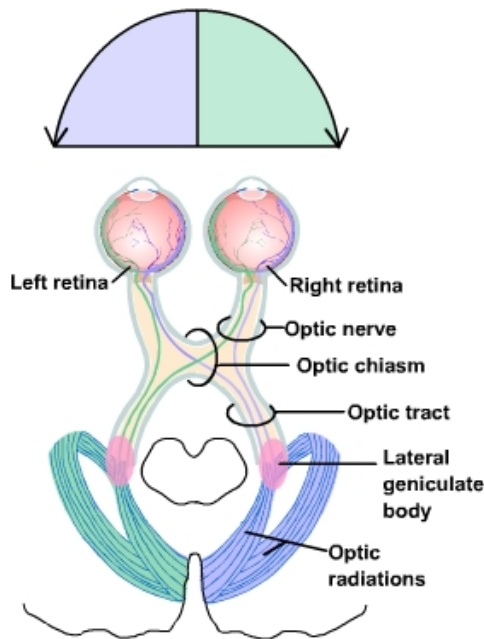


Figure 1.1: Illustration of the Visual Pathway and its components, including the course of information flow from the right (green) and left (blue) hemifields of the two eyes' visual fields. Adapted from [1].

etal cortex; the other pathway extends ventrally to terminate in the temporal lobe, including V4 and Inferior Temporal cortex (IT). It is suggested [3] that these two pathways serve different functions: the dorsal pathway is concerned with *where* an object is in visual space (motion, distance); the ventral pathway is concerned with *what* an object is (form, color, texture, all of which are involved in object recognition) (see Figure 1.2).

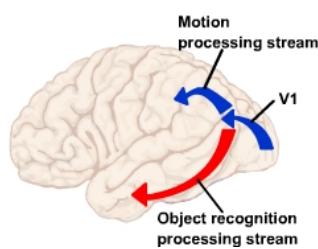


Figure 1.2: Distinction in the flow of visual information from the V1 to other cortical areas. The ventral stream transfers information to the inferior cortical areas, whereas the dorsal stream transfers it to the more superior cortex. Adapted from [4].

They then enter the optic canal, a bone-encased tunnel intended to protect the nerve, exit into the middle cranial fossa to form the intracranial part of the optic nerve, which continues till the two optic nerves join together to form the optic chiasm directly behind and above the pituitary stalk. Beyond the chiasm, the pathway continues as two distinct tracts, each carrying the temporal fibers from the other eye. The optic tract then passes posteriorly where most of the axons synapse in the layers of the Lateral Geniculate Nucleus (LGN) of the midbrain, which is a posterolateral extension of the thalamus.

The majority of the fibers pass posteriorly to become the genico-calcarine tracts, which have both parietal and temporal loops and terminate into the cuneus gyrus and lingual gyrus of the primary visual cortex, respectively (see Figure 1.1). Perception of sight ultimately derives from processing within this and adjacent areas of the brain [2].

1.2.2 Information Processing In The Visual Cortex

The modules that compose the visual pathway from the retina to higher visual centers follow two diverging streams in the cortex: one pathway extends dorsally to terminate within the parietal lobe, including the motion detection area, Middle Temporal visual area (MT), and the visual areas of the posterior pari-

etal cortex; the other pathway extends ventrally to terminate in the temporal lobe, including V4 and Inferior Temporal cortex (IT). It is suggested [3] that these two pathways serve different functions: the dorsal pathway is concerned with *where* an object is in visual space (motion, distance); the ventral pathway is concerned with *what* an object is (form, color, texture, all of which are involved in object recognition) (see Figure 1.2).

The V1 area of the brain is involved in the initial cortical processing of all visual information necessary for visual perception. The color, shape and movement information from the thalamus are sent to different neurons within V1 for further processing and then sent onto different areas of the extrastriate visual cortex. Within V1, information processed by blob cells is used in color perception, color discrimination and the learning and memory of the color of objects. The blob cells are the "color" processing cells of the V1. On the other hand, V1 interblob cells belong in one of two categories: The first are location specific cells, which respond best when the stimulus is in a specific location of the receptive field. The information processed by these cells is used in object perception, discrimination, learning and memory, or in spatial orientation. These cells are the "shape, form and location" cells of the V1; The second kind of interblob cells is the movement sensitive ones, which respond best to moving stimuli and are utilized to detect object movement, direction and velocity and to guide eye movements. These are the "motion detecting" cells of V1.

The V1 sends input to the extrastriate visual cortex, which includes all the occipital lobe areas surrounding the V1. The extrastriate cortex in non-human primates has been subdivided into as many as three functional areas, V2, V3 and V4. The information corresponding to each of the aforementioned categories of neurons in the V1 is sent

to different areas of the extrastriate visual cortex.

Specifically, the neurons in the inferior temporal visual association cortex, i.e., the ventrally located neurons accessed by the ventral stream, are responsible for processing information necessary for our abilities to recognize objects and colors, read text and learn and remember visual objects. It can thus be concluded that, in the context of this thesis, which investigates task-evoked visual stimulation, this area of the brain will be the region of interest. More deliberately, four regions of extrastriate cortex are of utmost importance for the purposes of this current dissertation: the FFA, the Parahippocampal Place Area (PPA), the Lateral Occipital Cortex (LOC) and the Extrastriate Body Area (EBA).

1.2.3 Category-Specific Information Processing Areas In The Extrastriate Visual Cortex

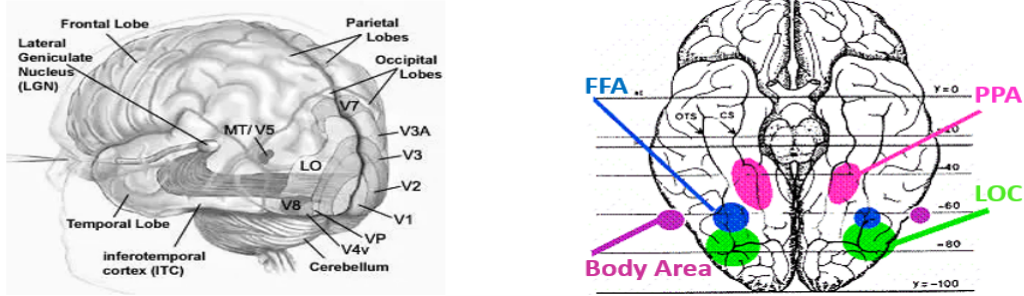
In the early 1990s, Positron Emission Tomography (PET) demonstrated activation of the ventral visual pathway, especially the Fusiform Gyrus (FG), in a variety of face perception tasks [4], [5]. fMRI studies of the specificity of these cortical regions for faces began with demonstrations of fusiform regions that responded more strongly to faces than to letter strings and textures [6], flowers [7] and other mixed stimuli [8]. Although face-specific fMRI activations could also be seen in many subjects in the region of the Superior Temporal Sulcus (STS) and in the occipital lobe in a region named the Occipital Face Area (OFA), the most consistent and robust face-selective activation was located on the lateral side of the mid-fusiform gyrus, within the IT, in a region consequently named the FFA. With the methods currently used, this region can be functionally identified in almost every normal subject in a short "localizer" fMRI scan contrasting the response to faces versus objects [9].

Another well studied category-selective region of cortex is the PPA, responding strongly to a wide variety of stimuli depicting places and/or scenes (e.g. outdoor and indoor scenes and houses) compared to various control stimuli such as faces or scrambled scenes [10]. Additionally, it has been found that PPA activity is not affected by the subject's familiarity with the place depicted, does not increase when subjects experience a sense of motion through the scene, and is greater when viewing novel versus repeated images [11]. Using sets of scenes that had viewpoint changes, it was demonstrated that the PPA treated scenes with viewpoint changes as different [12], suggesting that this area represents scenes as individual snapshots of each view rather than as a broader scene that integrates multiple similar snapshots. However, when subjects saw different snapshot views from panoramic scenes, which represented clearly different views but appeared to come from the same scene, fMRI showed no attenuation for panoramic repeats in the PPA, suggesting viewpoint-specificity [13].

The LOC is located on the lateral bank of the FG, extending both ventrally and dorsally, consisting of the Middle Occipital Gyrus (MOG) and the Inferior Occipital Gyrus (IOG) as well as the Lateral Occipital Sulcus (LOS) between them. This region has been shown to respond more strongly when subjects passively view photographs of common everyday objects than when they view visual textures without obvious shape interpretations [14]. Importantly, the magnitude of the response was no different for familiar objects and unfamiliar ones with clear three-dimensional shape interpretations (e.g. Henry Moore sculptures). A similar result was found using line drawings [15]: stronger responses to three-dimensional objects depicted in line drawings, whether familiar or novel, compared to scrambled line drawings. Several more studies provide evidence that the entire LOC region responds more strongly to intact objects with clear shape interpretations, than to control stimuli that do not depict clear shapes [16]–[18].

Since the turn of the twentieth century, neuroimaging studies have identified two brain regions of the extrastriate visual cortex that are highly sensitive to the perception of human bodies and body parts in comparison to other classes of stimuli. These regions are the EBA, which is a body-selective focal region located partly at both the posterior inferior temporal sulcus and the middle temporal gyrus [19] and the Fusiform Body Area (FBA) found ventrally in the fusiform gyrus [20]. Evidence derived from fMRI studies has shown that both areas become significantly activated in response to body and body parts stimuli visually presented in different formats such as photos, line drawings, stick figures and silhouettes compared to control stimuli like faces, tools and scenes [21]–[23]. Additionally, research seems to suggest that the EBA also

participates in more complex functions like body discrimination of self versus others. [24]. It has been suggested that EBA and FBA can be functionally dissociated, with a more selective activation for local body parts in EBA relative to more holistic images of the human body in FBA [25].



(a) Graphic of the visual areas of the brain thought to be geographically within the occipital lobe [26]. Adapted from Perez et al. [27].

(b) Brain diagram including some category-specific information processing areas of the brain [28]. Adapted from [29].

Figure 1.3: Illustration of Regions of Interest (ROIs) in the human brain.

While it has been clearly established that certain areas of the extrastriate visual cortex process category-specific information (see Figure 1.3), another critical inquiry, particularly in the context of fMRI MVPA of contrasts among different classes of stimuli, is whether each region is exclusively selective for target-specific stimuli or if there is overlap between regions, especially considering the close proximity among them. One such case is the FFA and FBA, which have been found in many subjects to be adjacent or overlap with one another. However, in ROIs that omit overlapping voxels it has been demonstrated [30] that, FFA showed no response above control objects for body stimuli and FBA showed no response above control objects for face stimuli, confirming strong selectivities in distinct but adjacent regions in the FG. Similar conclusions of high selectivity have been reached [31] in regard to the FFA and the PPA, where results revealed distinct response properties between the two regions for faces and houses respectively, implying a combination of spatially discrete domain-specific and relatively distributed domain-general organization mapping in the human ventral temporal cortex.

Many brain imaging tools are available to cognitive neuroscientists, including PET, Near Infrared Spectroscopy (NIRS), Magnetoencephalogram (MEG), Electroencephalography (EEG) and fMRI [32]. Some of those have had their time in the spotlight in the previous decades but have now been overshadowed by the more advanced, non-invasive neuroimaging techniques such as EEG and fMRI, which allow researchers to directly observe brain activities while subjects perform various perceptual, motor or cognitive tasks. It is therefore imperative that we acquire at least a basic understanding of the procedures and metrics through which these techniques work if we are to be able to interpret their results and further analyze them. For the purposes of this paper, we focus on the inner workings of fMRI, which is the instrument used to extract the data used in our MVPA.

1.3 Mechanisms of Functional Magnetic Resonance Imaging

1.3.1 Fundamentals of NMR Signal Generation

The outline of the process by which fMRI signal is generated begins with the scanner creating a powerful magnetic field \vec{B}_0 . All magnetic moments of nuclei with nonzero spin, including protons which are found overwhelmingly in the form of hydrogen nuclei in the human brain, tend to weakly align with \vec{B}_0 , creating a net macroscopic magnetization \vec{M}_0 . A coil within the machine, then transmits a radio frequency (RF) transverse magnetic field at the resonant frequency $\omega_0 = \gamma \cdot B_0$, where γ is the gyromagnetic ratio, tipping the magnetic moment from alignment and causing it to precess around the \vec{B}_0 axis at angular frequency ω_0 . For protons,

$\gamma = 2.675 \times 10^8 \text{ rad T}^{-1}$ and at a typical magnetic field strength of 3 T, the precession frequency $\nu_0 = \omega_0/2\pi$ is approximately 128 MHz. Following this interaction, the net magnetization vector can be described as two components: the remaining longitudinal magnetization along the \vec{B}_0 axis; and the rotating transverse magnetization perpendicular to \vec{B}_0 . The rotating component generates an oscillating magnetic field that induces a current in a nearby coil, thereby producing the basic measured Nuclear Magnetic Resonance (NMR) signal. Over time, the transverse magnetization decays exponentially with a characteristic time constant T_2 , and the longitudinal magnetization recovers exponentially towards its equilibrium value M_0 with a time constant T_1 [33], [34].

1.3.2 Relaxation Time Constants

T_1 relaxation is the process by which the z component of the net magnetization M returns to its initial maximum value M_0 parallel to B_0 . It can be modeled as a simple exponential with T_1 as a first-order time constant, defining it as the time required for M_z to reach $(1 - \frac{1}{e})$ or about 63% of its maximum value (see Figure 1.4 [35]). A typical value for T_1 , inside a 3 T magnetic field, in gray matter of the human brain is about 1.0 s. As M_z grows toward M_0 the energy of the spin system decreases, considering that more spins statistically favor the spin-up parallel orientation, which is the lower of the two potential energy states. Consequently, as T_1 relaxation occurs, energy dissipates from the system in the form of heat, hence the synonym for T_1 relaxation, "thermal relaxation". This heat is then transferred to nearby nuclei via collisions, rotations, or electromagnetic interactions, and becomes unrecoverable. At its core, T_1 relaxation represents an energy exchange process between spins and their external environment.

Blood inflow and Cerebral Blood Flow (CBF) can act to decrease the T_1 values of blood and extravascular tissue components, resulting in a modified, measured T_1 constant, termed T_1^* . Flowing blood moves spins from outside the imaging plane into the slice pixels. When spins in the imaging plane are saturated, signal from the unsaturated inflowing blood is enhanced relative to the surrounding stationary spins. The magnitude of this inflow contribution in vessels depends on the Magnetic Resonance Imaging (MRI) parameters, TR and flip angle θ . When the TR is sufficiently long to allow arterial blood spins from outside the imaging slice to flow into capillaries and exchange with extravascular tissue water, spatially specific perfusion contrast appears. In the extravascular tissue pool, $\frac{1}{T_1^*} = \frac{1}{T_1} + \frac{f}{\lambda}$ where f is the CBF and λ is the blood-to-tissue partition coefficient [36].

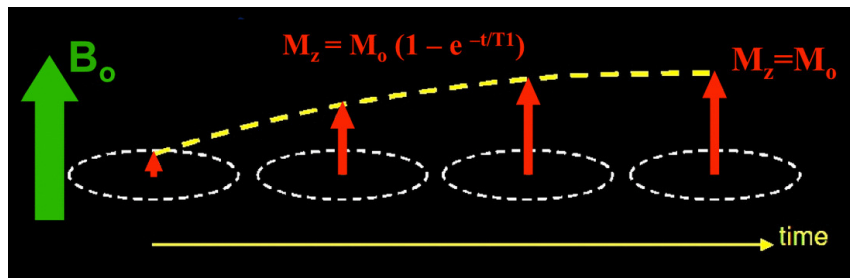


Figure 1.4: Illustration of T_1 relaxation. Adapted from [35].

T_2 is the time constant for decay or dephasing of transverse magnetization M_{xy} and may occur with or without energy transfer. T_2 relaxation is considered to follow first order kinetics, resulting in a simple exponential decay (identical to radioactive decay), resulting in T_2 being the time required for the net transverse magnetization to fall to $\frac{1}{e}$ or approximately 37% of its initial value [37]. Following a 90° RF pulse, the initial Boltzman distribution of spins in the z direction, constituting M_z , is preserved and transformed by the rotation into what is termed "phase coherence" in the xy plane, in the form of an asymmetrical clustering of spins which gives rise to a net transverse magnetization M_{xy} . After the pulse is over, the many transverse spin components will precess within the plane at the Larmor frequency. The presence of a non-zero M_{xy} at any time, is evidence of persistent asymmetry of transverse components of

angular momentum. Any process that disrupts either the number or the relative positions of said components will result in T2 relaxation. These fall into one of two general categories.

The first kind of T2 relaxation is when it accompanies T1 relaxation. If energy radiated during the latter, were to affect one of the spins contributing to M_{xy} , both its angular momentum components would be randomly changed, and it would immediately lose phase relations with other spins, thus it would stop contributing to M_{xy} altogether. As a result, M_{xy} would be diminished, meaning T2 relaxation would have occurred. We can conclude that any process causing T1 relaxation also results in T2 relaxation, while the opposite is not true. This is sometimes called the T1 contribution to T2 and explains why T1 needs to be monitored as well, even though it is the sweep of the transverse magnetization alone that induces a current in the receiver coils, ultimately producing the NMR signal.

On the contrary, stand-alone T2 relaxation is referred to as the secular contribution to T2. One of the most common ways for this to occur is when a spin is situated in a molecular environment where it experiences a local static magnetic field disturbance B_{loc} in addition to B_0 . The component B_{loc-z} of the secondary magnetic field, parallel to the main field, is added to the total magnetic field experienced by the spin, causing it to precess at a frequency $\omega'_0 = \gamma \cdot (B_0 + B_{loc-z})$. Meanwhile, the unaffected spins continue to precess at the original Larmor frequency. Over time, a phase difference of $\phi = \gamma \cdot B_{loc-z} \cdot t$ develops between the disturbed spin and the rest, leading to loss of phase coherence, T2 relaxation, and reduction in M_{xy} . Secular T2 relaxation can also occur due to a special dipolar interaction, where a pair of spins simultaneously exchange their longitudinal angular momentum components, resulting in no net T1 effect but loss of T2 coherence. In gray matter in the human brain, at a field strength of 3 T, measured T2 is around 0.1 s.

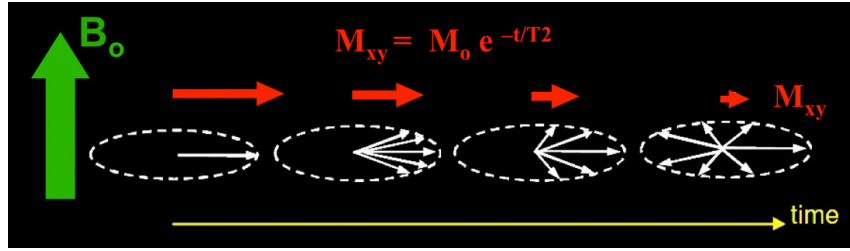


Figure 1.5: Illustration of T2 relaxation. Adapted from [37].

It needs to be noted that in any real NMR experiment, the transverse magnetization decays much faster than would be predicted by natural atomic and molecular mechanisms; this faster rate is denoted $T2^*$. It can be considered as "observed" or "effective" T2, whereas the latter can be thought of as the natural T2 of the tissue being imaged. $T2^*$ is always less than or equal to T2 (see Figure 1.6). $T2^*$ results principally from inhomogeneities in the main magnetic field, which may arise from intrinsic defects in the magnet itself or susceptibility-induced field distortions caused by tissue or other materials within the field. Certain Magnetic Resonance (MR) sequences using gradient echoes and relatively long Time of Echo values are called T2-weighted (T2w) [38].

Pixel sizes in typical fMRI studies are a few millimeters; each pixel may therefore include blood, extravascular tissue, and CSF. Since arterial blood and venous blood have different T2 values, these should be considered separately, with the assumption that capillary content is partly arterial blood and partly venous blood. Thus, NMR signal intensity from a pixel is the sum of signals originating from multiple compartments with different spin density and relaxation parameters. The fMRI intensity S can be described as seen in Equation 1.1 [39].

$$S = \sum_i \rho_i \times V_i \times M_{ss,i} \times e^{-TE/T_{2,i}^*} \quad (1.1)$$

$$M_{ss,i} = \frac{(1 - e^{-TR/T_1^*}) \sin \theta}{1 - \cos \theta \times e^{-TR/T_1^*}} \quad (1.2)$$

Subscripts i indicate each compartment; ρ is the water proton spin density, directly related to water content in the tissue; V is the volume fraction, which is approximately 1% for arterial blood [40] and 2.5-3% for venous blood [41], [42]; M_{ss} is the steady-state magnetization given by Equation 1.2; TR is the repetition time; T_1^* is the apparent longitudinal relaxation time in the presence of inflow; and θ is the flip angle. It should now be evident that fMRI signal changes depend not only on imaging parameters, but also on biophysical responses that significantly affect these variables.

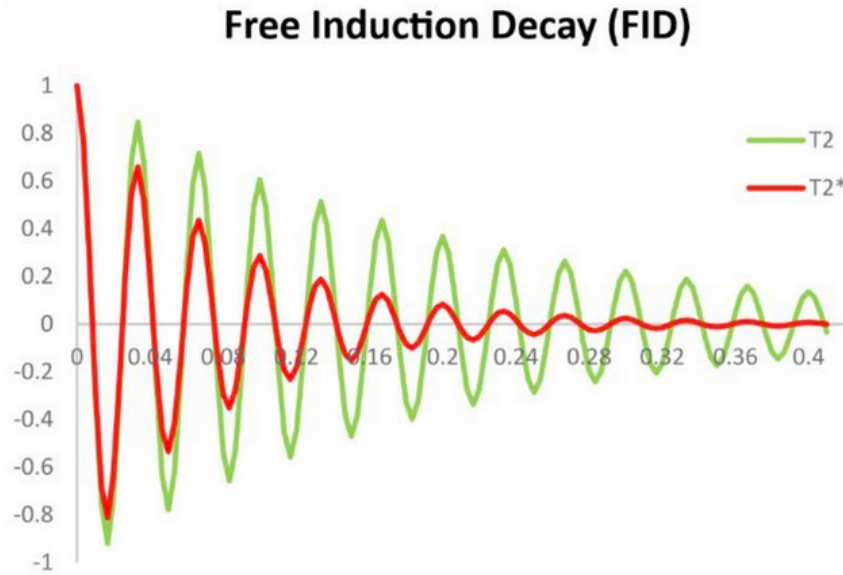


Figure 1.6: The observable NMR signal generated by non-equilibrium nuclear spin magnetization precessing about B_0 . Adapted from [43].

At this point, with a solid grasp of the general physical quantities involved in the production of NMR signals, it is important to link these quantities with biological processes in the human brain to progress from pure anatomical imaging to functional display. Several techniques can detect changes in metabolic activity following neural activation, including contrast fMRI, Blood-Oxygen-Level-Dependent (BOLD) fMRI, and perfusion fMRI. Contrast fMRI requires the injection of contrast agents such as iron oxide coated with sugar or starch. Although this method can provide relatively strong signals, researchers are often reluctant to use this semi-invasive method with healthy volunteers. Perfusion fMRI utilizes Arterial Spin Labeling (ASL) to magnetically label hydrogen nuclei in arterial blood and then images their distribution in the brain. The signal received from this technique is more stable and less noisy than that of BOLD fMRI, but it is also relatively weak, and the length of image acquisition time makes it impractical for many applications. Currently, the most widely used fMRI method is BOLD imaging.

1.3.3 Blood Oxygen Level Dependent (BOLD) Signal

The BOLD signal, captured in fMRI detects changes in deoxyhemoglobin (HbR) driven by localized changes in brain blood flow and blood oxygenation, which are coupled to underlying neuronal activity by a process termed neurovascular coupling. fMRI relies upon the measurement of T_2^* relaxation, which is sensitive primarily to local concentrations of paramagnetic HbR in venous blood, rendering the latter a naturally occurring contrast agent. Interpretation of the fMRI BOLD signal is intrinsically linked to understanding the underlying physiological and metabolic processes in the brain that modulate blood flow.

The BOLD effect related to neural activity arises because of two distinct phenomena. The first is that when hemoglobin (Hb)-the molecule in blood that carries oxygen-lose the oxygen to become HbR, its magnetic properties change in a subtle way: HbR is paramagnetic, and alters the magnetic susceptibility of blood, whereas Oxyhemoglobin (HbO) and the surrounding tissue

H₂O are diamagnetic (see Figure 1.7). The difference in susceptibility between blood vessels and the surrounding tissue creates local magnetic field distortions that decrease the net MR signal. In the brain, a typical Oxygen Extraction Fraction (OEF)-the fraction of O₂ carried by an element of blood that is removed in passing through the capillary bed-is approximately 40% and in a 3 T magnetic field this level of HbR in the veins and capillaries is sufficient to reduce the MR signal by about 10% in the baseline state, compared to what it would be if no HbR was present.

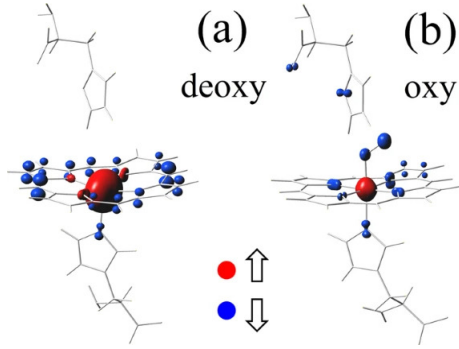


Figure 1.7: Illustration of magnetic-moment density $M(\mathbf{r})$ for the (a) HbR and (b) HbO heme clusters at $T = 150K$. The magnitude of $M(\mathbf{r})$ at an atomic site is proportional to the volume of the bubble at that site. Adapted from Fig. 2 p.2 Mayda et al. [44].

The combination of the aforementioned with the biophysical phenomenon, that when a brain area is activated, the blood flow increases-via a process called the hemodynamic response-to a greater degree than the oxygen metabolic rate, produces a useful basis for an experimental signal acquisition technique. The second phenomenon leads to a reduction in the OEF, a seemingly paradoxical scenario in which the venous blood is more oxygenated, despite the increase in oxygen metabolic rate, because the blood flow has increased to a greater extent. Taken together, these two phenomena produce the BOLD effect, a local increase in the MR signal due to a reduction in the OEF during increased neural activity. [33]

A prevailing misconception is that BOLD provides a direct measurement of neuronal oxygen consumption. However, this is generally not the case; classic positive BOLD signals, seen in response to functional stimuli, represent a decrease in HbR and thus an overoxygenation of the responding region [45]. These positive

BOLD responses correspond to a local, actively actuated, increase in blood flow and volume, which brings blood in sufficient excess to increase local oxygenation levels [46]. This response typically begins within about 500ms and peaks 3 to 5 seconds after stimulus onset Figure 1.8, even for short stimuli lasting less than 1 second, with more complex dynamics for prolonged stimuli.

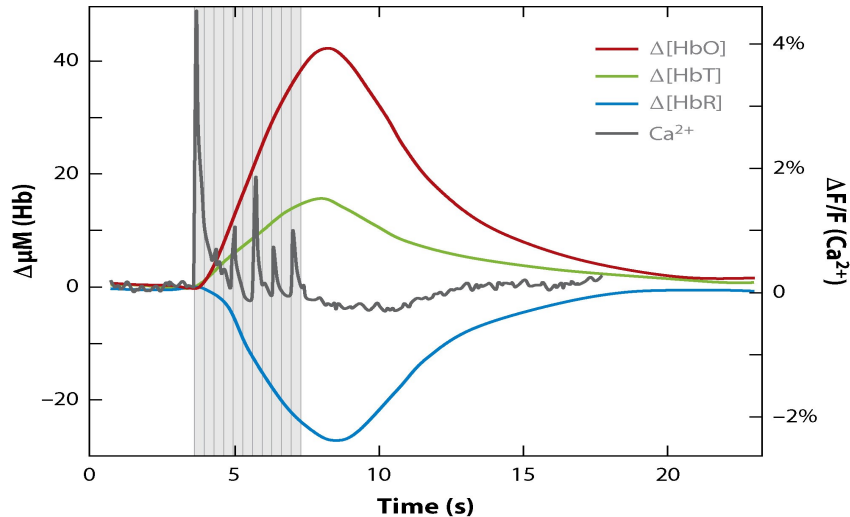


Figure 1.8: Stimulus-evoked response in somatosensory cortex of rats. Notably, there is a distinct increase in total hemoglobin (HbT) corresponding to vessel dilation and an increase in the number of red blood cells per unit volume of cortex, consistent with an increase in blood flow. HbO increases while HbR decreases, indicating a net overoxygenation of the region. The fMRI BOLD is sensitive to changes in HbR, where stimulus-evoked “positive BOLD” corresponds to the decrease in HbR shown here. Adapted from Fig. 2 p.4 Hillman et al. [47].

A range of cellular mechanisms, including astrocytes, pericytes, and interneurons, have been proposed to play a role in neurovascular coupling.[\[48\]](#) For classical interpretation of BOLD signals, it is assumed that neurovascular coupling is so robust that any increase in neuronal activity generates a proportional increase in local blood flow, irrespective of brain region, brain development, and pathological state [\[49\]](#).

This page intentionally left blank.

Chapter 2

Data Acquisition and Manipulation

2.1 The Human Connectome Project (*HCP*)

The data handled in this project has been amassed through the HCP. The HCP was an ambitious five-year effort to characterize brain connectivity and function and their variability in healthy adults. A consortium of investigators studied a population of 1200 subjects, using multiple imaging modalities along with extensive behavioral and genetic data. The imaging modalities included diffusion imaging (dMRI), resting-state fMRI (r-fMRI), task-evoked fMRI (t-fMRI), T1-weighted (T1w) and T2-weighted (T2w) MRI for structural and myelin mapping, plus combined MEG and EEG.

During the first phase, the WU-Minn HCP consortium made a major effort to improve the methods of data acquisition and analysis, since up to that point in time, despite their great promise, all of the modalities that could be applied to *in vivo* human connectomics had serious limitations in their sensitivity, accuracy and resolution [50]. This initial phase was followed by a three-year period of data acquisition from the main cohort [51]. A key objective was to understand inter-individual variability of brain circuits, including its genetic bases and its relation to behavior, rather than merely aiming to determine the average, or typical connectivity in healthy adults. This was achieved by sampling more than three hundred young adult sibships of average size 3-4, with most of these including a monozygotic (MZ) or dizygotic (DZ) twin pair. All subjects were between 22 and 35 years old, an age range chosen to represent healthy adults beyond the age of major neurodevelopmental changes and before the onset of neurodegenerative changes. While the HCP was cross-sectional, many participants were drawn from ongoing longitudinal studies [52], [53]; they had extensive previous assessment, particularly with respect to history of the presence or absence of emotional and behavioral problems.

As for the methods, Figure 2.1 provides a high-level view of the plans used for data acquisition in Phase II of the project. Each subject spent two days at Washington University (WashU) for: behavioral assessment, whose measures spanned a broad range in the domains of cognition, emotion, perception and motor function, and they were mainly drawn from the United States of America (USA) National Institutes of Health (NIH) but were supplemented by a number of complementary additional measures, blood draw for eventual genotyping, and four MR scanning sessions, with three lasting one hour. The scans at WashU were carried out using a customized 3 T connectome scanner adapted from Siemens Skyra, designed to improve the quality and resolution of connectivity data; a subset of 200 subjects was also scanned at University of Minnesota (UMinn) using a new 7 T system which offers advantages, especially for the resting and task-based fMRI studies, but also for diffusion-based techniques if sufficiently short echo times can be achieved for diffusion weighting. Both systems capitalized on major improvement in advanced MR pulse sequences to obtain dMRI, r-fMRI, and t-fMRI, plus T1w and T2w anatomical scans. The t-fMRI scans included a range of tasks aimed at providing broad coverage of the brain and identifying as many functionally distinct domains and cortical parcels as possible. A subset of 100 subjects was also studied with combined MEG and EEG at Saint Louis University (SLU), which offer much better temporal resolutions (ms instead of s)

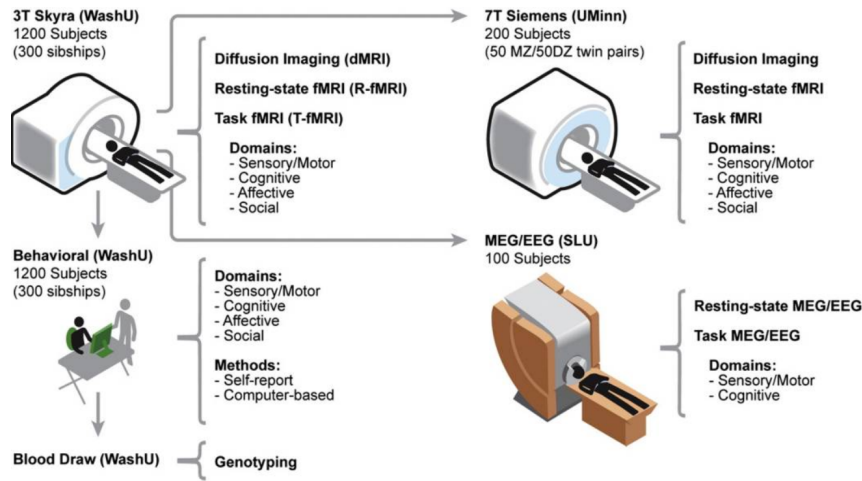


Figure 2.1: Schematic summary for acquiring imaging, behavioral, and genetic data using MR and MEG/EEG scanners at three HCP sites. Adapted from [54].

but lower spatial resolution than MR.

2.1.1 Task-fMRI Battery of the HCP

The HCP used t-fMRI to help delineate the relationships between individual differences in the neurobiological substrates of mental processing and both functional and structural connectivity [54]. We know that there are important individual differences in the patterns of connectivity even among persons with no diagnosable neurological or psychiatric disorders, and there is increasing evidence that this variability is associated with alterations in cognitive and behavioral variables that constrain real world function [55]–[57]. For example, higher intelligence quotient (IQ) among healthy adults is associated with shorter path length and higher global efficiency in measures of brain functional connectivity [58] as well as greater global connectivity in prefrontal cortex [59], thus providing evidence that more efficient connectivity contributes to more effective cognitive function. As another example, developmental research is increasingly suggesting that maturation of functional and structural networks in the human brain underlies key aspects of cognitive and emotional development [60]–[66].

The goal for the HCP was to identify and utilize a reliable and well-validated battery of measures that assess a wide range of human functions and behaviors in a reasonable amount of time (3–4h), to satisfy subject burden considerations. The base for the HCP’s assessment was the set tools and methods developed by the NIH Toolbox of Assessment of Neurological and Behavioral function [67], including tasks developed and validated using item response theory and computer adaptive testing where appropriate and feasible. The battery was additionally expanded with tests to include measures of the following domains not covered by the Toolbox: 1) subthreshold symptoms of mood, anxiety and substance abuse; 2) additional measures of visual, memory and emotion processing; 3) personality; 4) delay discounting, as a measure of self-regulation and neuroeconomic decision-making [68], [69]; 5) fluid intelligence as a measure of higher-order relational reasoning that has been linked to important individual differences in both life function and brain function [70]; 6) menstrual cycle and hormonal function for women; and 7) sleep function, which may be highly relevant to understanding individual differences in behavior.

The choice of t-fMRI tasks was driven by the following considerations. The aim was to identify nodes: 1) in well-characterized neural systems; 2) in as wide a range of neural systems as possible; 3) with activation locations that are reliable over time in individual subjects; 4) with activations consistently detectable in most individuals (sensitivity); and 5) that are associated with a broad range of cognitive and affective processes of interest to the NIH Blueprint Institutes. In addition, it was necessary that a subset of the tasks must be suitable for task-evoked MEG (T-MEG).

Initial piloting targeted a broad range of domains that sampled diverse neural systems of interest to a wide range of individuals in the field, including: 1) visual and somatosensory-motor systems; 2) category-specific representations; 3) language function (semantic and phonological processing); 4) attention systems; 5) working memory/cognitive control systems; 6) emotion processing; 7) decision-making/reward processing; and 8) episodic memory systems.

2.1.2 Working Memory Task of the HCP

The data which is presently being examined was drawn from the WM-task, which was combined with category-specific representation tasks into the following, single task paradigm [71]. One can ignore stimulus type and focus on only memory load comparisons to identify dorsal-frontal and parietal regions involved in working memory and cognitive control. Alternatively, one can collapse across memory load and focus only on stimulus type comparisons to identify temporal, occipital and parietal regions that respond to specific stimulus types.

Stimuli were projected onto a computer screen behind the subject's head within the imaging chamber. The screen was viewed by a mirror positioned approximately 8 cm above the subject's face. Participants were presented with blocks of trials that consisted of pictures of places, tools, faces and body parts (non-mutilated parts of bodies with no "nudity"). Within each run, the four different stimulus types were presented in separate blocks. Also, within each run, half of the blocks use a 2-Back WM-task and half use a 0-Back WM-task (as a working memory comparison). In short, in "N-Back" tasks participants are presented a sequence of stimuli one-by-one. For each stimulus, they need to decide if the stimulus currently being displayed, belongs to the same category as the one presented N trials before. The factors that influence performance are not only the number N , but also the speed of presentation and the size of the set of stimuli. A 2.5 s cue indicated the task type (and target for 0-Back) at the start of the block. Each of the two runs contained eight task blocks (10 trials of 2.5 s each, for 25 s) and four fixation blocks (15 s). On each trial, the stimulus is presented for 2 s, followed by a 500 ms inter-task interval (ITI). The procedure is showcased in time order in Figure 2.2.

The following event-related contrasts can potentially be generated between 2-Back and 0-Back tasks: 1) targets for the first are 2-Back repeats while for the second, they are targets that match the cue stimulus; 2) non-targets are novel items for the former and targets that do not match the cue stimulus for the latter; and 3) lures are 1-Back and 3-Back repeats for the 2-Back tasks and repeated stimuli that do not match the cue stimulus, for 0-Back tasks.

The task design outlined above is expected to reveal distinct patterns of behavior, performance, and consequently brain activation among subjects. While there will be considerable overlap in these patterns, analysis can isolate the unique aspects, resulting in consistent and distinguishable fMRI signal from specific brain areas in response to category-specific stimuli. This pattern recognition and screening from the selection of patterns that stood out, could enable the classification of certain brain regions as more responsive and associated with processing specific types of information.

Segment Type	Duration (s)	N-Back Paradigm	Target Category
Setup	10	-	-
Cue	2.5	-	-
Task	25	2-Back	Body
Cue	2.5	-	-
Task	25	0-Back	Face
Fixation	15	-	-
Cue	2.5	-	-
Task	25	2-Back	Tools
Cue	2.5	-	-
Task	25	0-Back	Body
Fixation	15	-	-
Cue	2.5	-	-
Task	25	0-Back	Place
Cue	2.5	-	-
Task	25	2-Back	Face
Fixation	15	-	-
Cue	2.5	-	-
Task	25	0-Back	Tools
Cue	2.5	-	-
Task	25	2-Back	Place
Fixation	15	-	-

Figure 2.2: Display of the exact sequence of events during the WM-task paradigm.

2.2 Analysis of fMRI Signal

In the analysis of fMRI signals, the primary output is a samples-by-features data matrix, similar in structure to conventional table matrices with rows and columns. Each feature represents a voxel in the brain image, and their maximum number depends on the protocol used during the fMRI scan, determined by the institution that collected the data, not by the data users. Samples are created based on the researcher's design of the analysis. Each vector of data over multiple voxels for a single sample is called a pattern, and each cell contains information that integrates the BOLD signal data as well as the researcher's analysis parameters.

The BOLD signal captured by the fMRI machine undergoes a series of processing steps unique to each analysis, resulting in varied outcomes. These outcomes are shaped by the researcher's choices, which are tailored to address the specific goals and inquiries of the research. These processing steps, which are detailed in subsection 3.2.2, replace the BOLD in each cell of the data matrix with a statistical value that reflects both the signal's characteristics and the researcher's decisions.

At first glance, a samples-by-features matrix might seem to represent a two-dimensional analysis, but it is far more intricate. Each cell may contain data points that incorporate a single or multiple explanatory variable (EV)s meaning each data point can be a function of several variables rather than a constant for each voxel. Additionally, sample attributes can further increase the number of variables included. These attributes, which function as headers of either rows, columns or the entire table, include crucial information such as the target stimulus that produced the corresponding pattern, and the chunk to which the pattern belongs. Patterns from different chunks are considered independent of each other. Researchers may designate sample attributes differently based on logical assumptions, which can yield different practical conclusions and potentially increase the degrees of freedom in the analysis. Such a practice is shown in detail in subsection 3.3.2.

Apart from technical decisions in data processing, the two main levers that can be manipulated are: 1) determining how many of the total EVs provided by the experiment design to include in the analysis and whether some variables can be grouped together based on the desired effect; and 2) establishing the correlation between these EVs.

2.2.1 Univariate Pattern Analysis

Univariate Pattern Analysis (UPA) is a statistical approach used in neuroimaging to analyse brain activity data, particularly focusing on individual voxels. This method examines each voxel independently, assessing how its activity varies in response to different experimental conditions. Technically, UPA measures the magnitude of an EV correlation paradigm, otherwise known as the contrast of explanatory variables (COPE) in each voxel independently. While UPA can calculate the mean and standard deviation of the activation pattern for each voxel, either across varying conditions or over time, it does not provide information about the overall distribution behavior or the joint probability and correlations between voxels.

For example, consider analyzing brain activity during all 0-Back trials featuring a face as a stimulus, with the only EV being the stimulus category. This analysis might show activation in both the V1 and the FFA during these trials. However, it cannot conclusively determine that these areas are more responsive to this stimulus category. By averaging the signal for this case and for three other identical UPAs with different stimulus categories, one might conclude that the V1 area, showing similar activation across all categories, is not involved in category-specific information processing but is generally activated when the subject observes anything. Nevertheless, this claim would be weak, as UPA cannot distinguish what percentage of the signal magnitude is directly due to the stimulus category versus other factors.

UPA is straightforward and widely used due to its simplicity and ease of interpretation. It is particularly useful when incorporating a temporal element into the assessment, as the calculations for a more complex analysis over time can become excessive. However, UPA does not account for interactions between voxels, which can limit its ability to detect complex brain activity patterns and can lead to false or weak classification of brain activity patterns. Despite this

limitation, UPA remains a valuable tool for identifying localized brain responses and establishing a baseline for more complex analyses.

2.2.2 Multivariate Pattern Analysis (MVPA)

A more suitable tool for complex analyses and deriving concrete, all-encompassing conclusions would be Multi-Variate Pattern Analysis (MVPA). In the context of neuroimaging, MVPA is an advanced analytical technique that decodes intricate brain stimulation patterns by leveraging the joint probability distribution of voxel activities. It involves examining multidimensional probability functions that capture the interdependencies and correlations between multiple voxels simultaneously. By considering the multidimensional probability density function (PDF), MVPA can model the likelihood of observing specific activation patterns across a Region of Interest (ROI), thereby incorporating the covariance matrix to account for the pairwise correlations among voxels. This covariance structure enables the identification of distributed neural networks that co-activate in response to cognitive tasks.

More specifically, MVPA examines the entire spatial pattern of voxel activations, enabling the decoding of cognitive states, perceptual experiences, or experimental conditions from the distributed patterns of brain activity. This method can uncover intricate patterns and relationships that reflect complex neural processes.

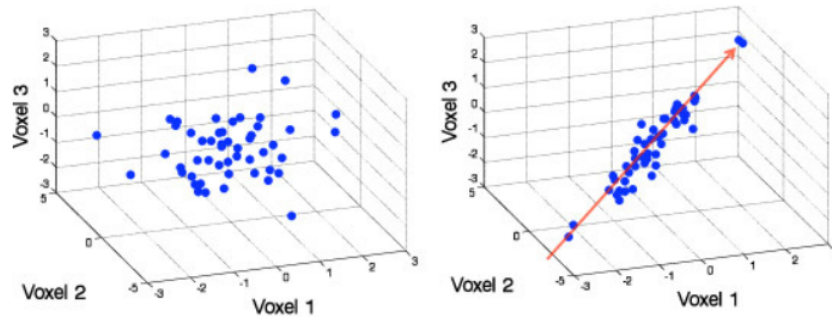


Figure 2.2: Description of the difference between UPA and MVPA. On the left, there is no correlation between the three variables plotted, while on the right one can see a major source of variance indicating a positive correlation between all three voxels. A UPA that just considered mean values on a voxel-to-voxel basis could not tell any difference between these two scenarios. In contrast, MVPA identifies the sources of variance indicated by the red arrow before proceeding to construct neural activation patterns from these sources. Adapted from Habeck et al. [72].

At its core, MVPA involves extracting patterns from fMRI or other neuroimaging data and applying machine learning algorithms to classify these patterns. Common classifiers used in MVPA include Support Vector Machines (SVMs), logistic regression, and neural networks, which can learn to distinguish between different cognitive states based on training data. By training these classifiers on labeled data, MVPA can predict the cognitive state of new, unlabeled data with high accuracy. MVPA also utilizes dimensionality reduction techniques like Principal Component Analysis (PCA) or Independent Component Analysis (ICA) to manage the high-dimensional nature of neuroimaging data, enhancing computational efficiency and reducing noise. Additionally, techniques like cross-validation are employed to ensure the robustness and reliability of the classifier's predictions.

2.2.3 Data Processing, Model Fitting and Classification

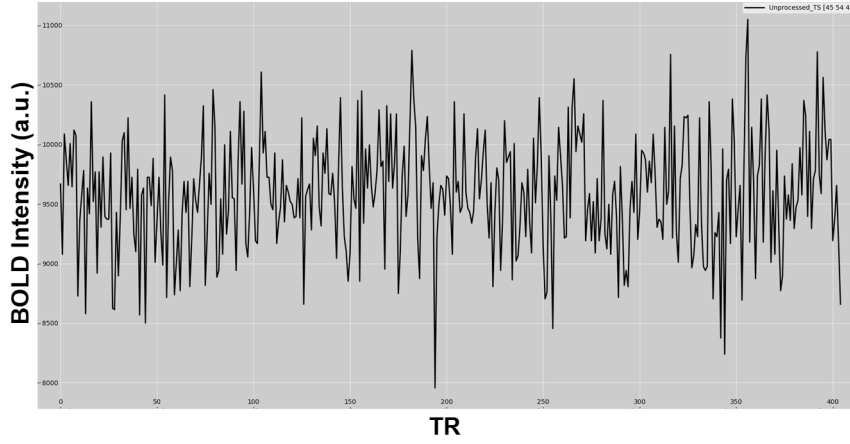


Figure 2.3: A snapshot of an unprocessed time-series.

The unprocessed BOLD signal is captured as a time-series (see Figure 2.3), representing the signal measured at each voxel throughout the entire fMRI run. Initially, this unprocessed time series is quite ragged, featuring high resolution but also substantial noise, often to the point where noise overshadows the signal. To enhance the signal-to-noise ratio, several preprocessing steps are taken, including skullstripping [73], motion correction using rigid-body transformations, slice-timing correction, high-pass filtering, and, most importantly, smoothing. Smoothing involves replacing the signal at each voxel with a weighted average of its neighbors, which reduces spatial resolution but significantly improves the signal-to-noise ratio. This process also facilitates the normalization of the subject's brain to a template brain with standardized coordinates using affine transformations. Once preprocessing is complete, the time series appears as shown in Figure 2.4.

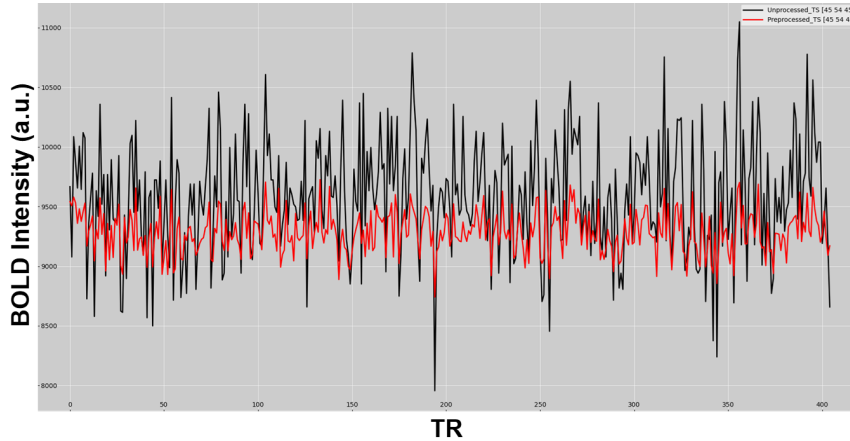


Figure 2.4: A snapshot of a pre-processed time-series.

Now the time series is ready for model fitting. To achieve this, an assumption has to be made as to the expected form of the BOLD response. Empirical studies [74], [75] demonstrated that, after a stimulus is presented, any responsive part of the brain exhibits an increase in BOLD signal. This response typically follows a consistent pattern, peaking around 6 s and then returning to baseline over the next several s. This shape can be modeled with a gamma distribution [76]. When the gamma distribution is parameterized to best fit the observed BOLD response observed by the majority of empirical studies, it is known as the canonical Hemodynamic Response Function (HRF). The HRF generated by a single impulse stimulus is illustrated in Figure 2.5a, while the HRF for a "boxcar" stimulus is shown in Figure 2.5b.



(a) The HRF generated by a single impulse stimulus. In this instance, the stimulus occurs at timepoint 0 on the x-axis. (b) The HRF generated by a "boxcar" stimulus lasting 15 s. Notably, the BOLD signal begins descending back to baseline around the 15 s mark.

Figure 2.5: Illustration of the fundamental HRF shapes. Adapted from [76].

Constructing a General Linear Model (GLM) to fit the data involves estimating the expected BOLD response by calculating the ideal beta weights for each regressor (EVs). The model is then fitted to the time-series at each voxel, producing a function known as the fitted time-series, as shown in Figure ??.

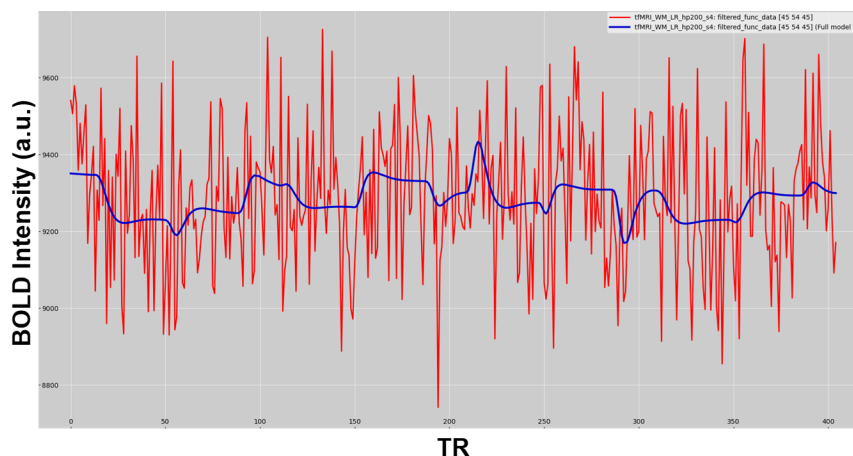


Figure 2.6: One instance of a fitted time-series, shown in red.

This overarching HRF, pertaining to one voxel and one COPE (number of regressors) at a time, serves as the unit of data that can be fed into a classifier. It is these fitted time-series, or rather the beta-weights that characterize them, that the classifier trains on and eventually bases its predictions on.

This page intentionally left blank.

Chapter 3

Methods

3.1 Pipeline Overview

The procedure followed in the current work is displayed in figure Figure 3.1.

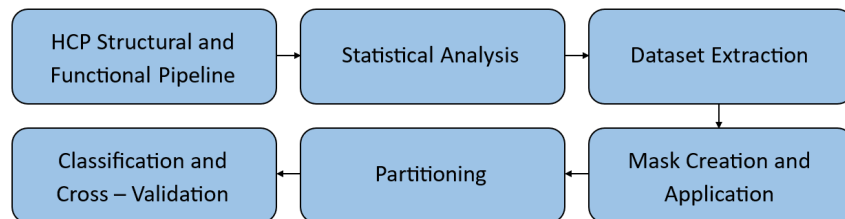


Figure 3.1: Pipeline Overview.

The starting point of the data was preprocessed WM task fMRI Neuroimaging Informatics Technology Initiative (NIFTI) files, which had undergone initial pre-processing steps included in the structural and then functional HCP pipelines [77] and were downloaded from the ConnectomeDB platform [78]. Twenty subjects, selected arbitrarily to balance a reasonable effect size with low computing power needs, were included as shown in figure Figure 3.2. For all analyses, NIFTI files from both Left to Right (LR) and Right to Left (RL) scans were included for all subjects. This LR and RL distinction was made to facilitate geometric distortion correction while simultaneously providing additional data points.

Subject IDs			
100307	100408	101107	101309
101915	103111	103414	103818
105014	105115	106016	108828
110411	111312	111716	113619
113922	114419	115320	116524

Figure 3.2: List of IDs for subjects initially chosen for all analyses.

3.2 Pipeline Segments

3.2.1 Preprocessing

All data processing was executed in FMRIB Software Library, abbreviated FSL (FSL v. 6.0.7.12, [79]). A single preprocessing setting was altered from those in the HCP pipelines: the spatial smoothing parameter. The dimensions of the rectangular smoothed voxel neighborhoods were changed from 5 mm to 4 mm. This adjustment improves the signal-to-noise ratio and is a widely used standard for relatively small ROIs, such as the FFA and PPA, which are examined in this study.

3.2.2 Statistical Analysis

Voxel-wise time-series were input into FMRIB's Expert Analysis Tool (FEAT). Based on the eight EVs established by the HCP pipeline (.fsf files) — two EVs for each stimulus category, one for 2-Back and one for 0-Back trials — new COPEs were designed. Two different analyses were conducted, both utilizing double-Gamma HRF convolution fitting:

Paste		Title	EV1	EV2	EV3	EV4	EV5	EV6	EV7	EV8
OC1	✓	BODY-AVG	0.5	-0.	-0.	-0.	0.5	-0.	-0.	-0.
OC2	✓	FACE-AVG	167	0.5	-0.	-0.	-0.	0.5	-0.	-0.
OC3	✓	PLACE-AVG	-0.	-0.	0.5	-0.	-0.	-0.	0.5	-0.
OC4	✓	TOOL-AVG	-0.	-0.	-0.	0.5	-0.	-0.	-0.	0.5

Figure 3.2: List of COPEs designed for all 2C analyses.

- I. In the first analysis, 4 COPEs (see fig. Figure 3.2) were parametrized to estimate the HRF corresponding to the average BOLD signal of each stimulus category, regardless of the N-Back paradigm used. The category-specific signal was averaged by including both 2-Back and 0-Back trials with equal weighting (50 – 50), and the signal from all other trials was subtracted using a factor of -0.167 ($1/6$).
- II. In the second case, the same approach was taken, but the signals from 2-Back and 0-Back trials for each stimulus category were considered independent, resulting in 8 COPEs (see fig. Figure 3.2). This decision was based on the fact that these blocks were always separated by tens of seconds. Thus, each EV's average signal was calculated while subtracting all other sources with a factor of -0.143 ($1/7$).

Paste		Title	EV1	EV2	EV3	EV4	EV5	EV6	EV7	EV8
OC1	✓	2BK_BODY-A'	1	143	143	143	143	143	143	143
OC2	✓	2BK_FACE-A'	143	1	143	143	143	143	143	143
OC3	✓	2BK_PLACE-I	143	143	1	143	143	143	143	143
OC4	✓	2BK_TOOL-A'	143	143	143	1	143	143	143	143
OC5	✓	0BK_BODY-A'	143	143	143	143	1	143	143	143
OC6	✓	0BK_FACE-A'	143	143	143	143	143	1	143	143
OC7	✓	0BK_PLACE-I	143	143	143	143	143	143	1	143
OC8	✓	0BK_TOOL-A'	143	143	143	143	143	143	143	1

Figure 3.2: List of COPEs designed for all 4C analyses.

A Unix shell script was created to automate FEAT analyses across all runs of all available subjects. The script requires only the original .fsf file, which contains the analysis design, as input. In the first case, each analysis produced 4 COPEs, resulting in 4 patterns per run (LR and RL) and 8 patterns per subject, generating a total of 160 patterns. In the second case, each analysis produced 8 COPEs, resulting in 8 patterns per run (LR and RL) and 16 patterns per subject, generating a total of 320 patterns.

It is important to note that the FEAT analysis is a single core process and the time required to complete is not bound on the number of COPEs included, but rather on the complexity of the COPE design and the quantity of voxels analysed. As a result, with the current hardware limitations and no parallel programming automation designed for this body of work, each analysis took an average of approximately 22 min in the first occasion and 16 min in the second, even though the number of COPEs was doubled in the latter.

3.2.3 Dataset Extraction - Construcion

All subsequent data analysis was conducted using custom code written in MATLAB (R2023b). A script was developed to extract patterns from each run for each subject, scalable to accommodate any name and number of subjects. All patterns were conjoined into a single dataset, with sample attributes assigned to them, including target, target label and chunk. The target refers to the stimulus category, numbered as follows: 1 for Body, 2 for Face, 3 for Place, and 4 for Tool, with the labels being the human-readable target names. Chunks are distinguished by a unique number, denoting pattern independence. This independence is crucial because it allows the classifier to train and test on disjoint sets of chunks, thereby avoiding circular analysis (double-dipping).

The analysis that merges signal from 2-Back and 0-Back trials resulted in 2 chunks per subject and shall be referred to as analysis 2C. The analysis that separates the signals from different N-Back paradigms produced 4 chunks per subject and will therefore be called 4C.

3.2.4 Mask Creation - Application

Once the data was fully processed, two masks were created to distinguish data pertaining to the FFA and the PPA. These masks, which are logical matrices applied to the dataset to exclude any data outside the selected ROI, were "circular", though pixelated, with a radius of 12 voxels, containing a total of 1,416 voxels. Mask centers were determined using Neurosynth's Locations Tool (see [80]) and identified as [40, -52, -20] for the FFA and [26, -33, -19] for the PPA, in MNI152 coordinates. The radius was specifically chosen to maximize ROI volume (ensuring the intended brain region is within the ROI for all subjects) while preventing overlap between brain regions that process different category-specific information, as shown in figure (Figure 3.2).

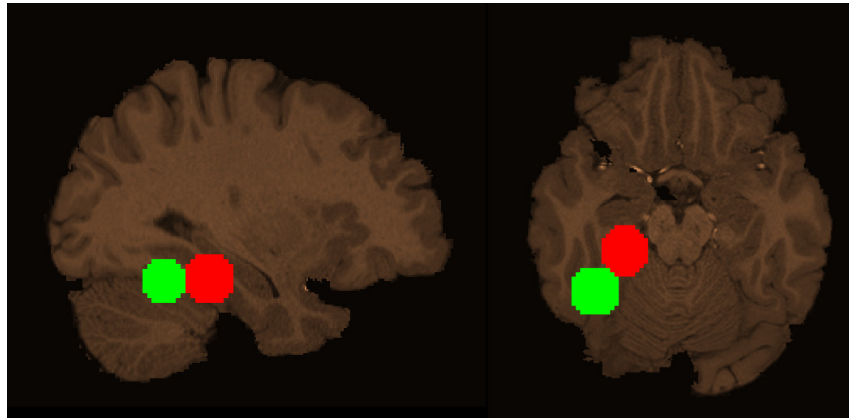


Figure 3.2: Illustration of FFA and PPA ROIs after mask application, at the sagittal and transverse planes. Notably, there is no overlap between the two areas, even when they are at their maximum extent.

It should be noted that this is the first point at which the sheer volume of data can be reduced without loss of potentially crucial information. The initial dataset contained patterns for all 902,629 voxels, depicting signal for the entire brain. After the FFA and PPA masks were applied, the non-zero signal voxels included in the masked datasets were 925 and 888 respectively, allowing for a much faster, more efficient and more intricate manipulation of the data.

3.2.5 Partitioning of Masked Dataset

For classification, the data must be split into independent training and test sets. A script was developed to partition the masked dataset with a variable train/test split ratio. To facilitate cross-validation, the script can produce a specified number of folds, each containing unique combinations of patterns within training and test datasets. The classifier can be run on any

number of these partitions, resulting in a mean accuracy that reliably reflects the classifier's predictive ability, independent of any single partitioning scheme. Partitioning was conducted with the CoSMo MVPA `independent_sample_partitioner` command [81], following the appropriate manipulation of the dataset.

3.2.6 Classifier Training and Testing (MVPA)

Classification is a supervised machine learning method in which the model predicts the correct label for a given input based on an algorithm that recognizes patterns associated with each label. In this study, the classifier functions as an 'eager learner,' creating a model and making future predictions based on this model, rather than continuously comparing test data to training data. A descriptive illustration of the process can be seen in Figure 3.3.

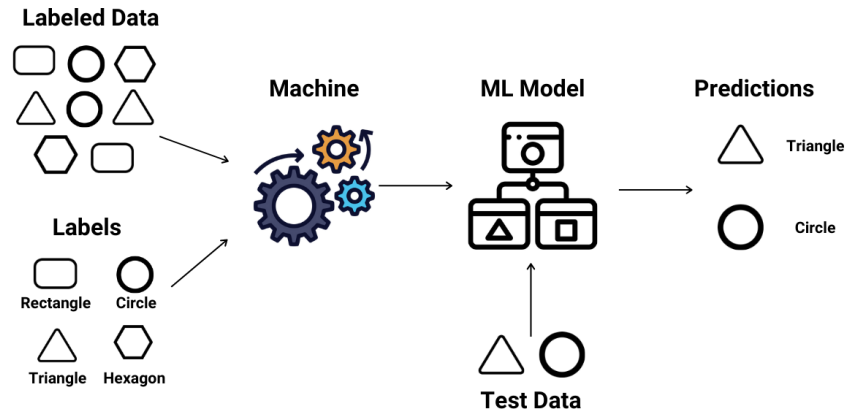


Figure 3.3: Supervised Learning Classification Illustration. Adapted from [82].

In this case, classification was conducted using the CoSMo MVPA `cosmo_classify_libsvm` command [83] which utilizes a SVM algorithm [84].

3.3 Data Analysis

The classifier's accuracy was treated as a function of three variables, with all other parameters staying constant. The three variables were: 1) number of chunks of data per subject; 2) fold count; and 3) subject count.

3.3.1 Category-Specific Baseline Brain Activation (UPA)

The first step in facilitating further analysis is the Univariate Pattern Analysis (UPA) of the baseline brain activation signal for each stimulus category in both regions. For each region, the statistical *b*-value assigned to each cope after the FEAT analysis was used as an indicator of the baseline signal magnitude. The mean of the square of all values associated with each stimulus category was calculated to account for both positive and negative values. Consequently, the means for all 2C analyses were derived from 40 patterns, while for 4C, they were derived from 80 patterns, corresponding to the number of target-pattern pairs in each dataset. The results were presented in bar plots.

Additionally, an extra analysis was conducted for the FFA, using cope values derived from a FEAT analysis of a smaller, more central FFA region with a radius of 6 voxels around the center, compared to the 12-voxel radius used previously. This approach aimed to clarify the relationships among the various signals, as they are expected to be more robust in this more focused area.

3.3.2 Classifier Performance - Chunks per Subject

The WM task paradigm used in the HCP limits the maximum number of chunks per subject to 4, as trials within the same stimulation block (without intermittent fixation blocks) cannot be considered independent, and subjects participated in a total of 4 active trial blocks. However, the minimum number of chunks per subject can be as low as 1, effectively treating all trials as subject-dependent. The choice of chunk count depends on the researcher's approach and objectives.

- I. In analysis 4C all blocks were considered independent as long as they involved a different N-Back paradigm and were separated by at least one fixation block. A total of 80 chunks were assigned to the 320 patterns, with each chunk containing 4 patterns, one for each target.
- II. In analysis 2C the N-Back paradigm restriction was lifted. Signal from the same target's 2-Back and 0-Back blocks was placed in the same chunk, resulting in 40 chunks for all 320 patterns, with each chunk containing 8 patterns. Essentially, these chunks represent different runs, with two for each subject, totaling 40 chunks.

3.3.3 Detecting Outlier Subjects

The first step in data manipulation following FEAT analyses was to identify any individual subjects whose data stood out as irregular. Considering our analysis focuses on the Fusiform Gyrus in the right hemisphere only, subjects who predominantly show activation in the left hemisphere could potentially dilute the classifier's data pool. The same issue can arise if a subject's data acquisition process contained artifacts. Determining outlier subjects is crucial before proceeding with further data analysis steps in order for the results to be reflective of the truth.

The 16 patterns corresponding to each subject in analysis 4C were individually run through the classifier, cross-validated with the maximum fold count of 4. In this process, 3 chunks (each containing 4 patterns) were used as training data, while the remaining chunk was utilized for testing. The mean accuracy of the classifier across all folds was calculated, and if it fell below 10%, the subject was excluded from the remainder of the analysis, since such low accuracy is attributed to the nature of the data and not the classifier's properties. Consequently, two subjects were excluded from both the FFA and the PPA analyses, as further explained in subsection 4.2.2.

These subject exclusions were applied to analysis 2C as well. Although the approach differs between N-Back trials for the same category-specific stimulus, the classifier's input remains fundamentally the same, so the characteristics that define a subject as an outlier are expected to remain consistent. Moreover, replicating the same analysis for 2C is impractical since each subject corresponds to only 8 patterns divided into 2 chunks. At best, this would allow for a 50/50 train/test split, where each dataset contains 4 patterns from different chunks. This split is far from ideal and does not accurately reflect the classifier's performance under the 80/20 ratio, which is utilized for all analyses to follow.

3.3.4 Classifier Performance - Fold Count

Cross-validation is essential for verifying the classifier's results, but it can also lengthen and complicate the process by introducing another variable: fold count. It's crucial to investigate this variable to determine the optimal number of folds for practical, repetitive analyses, as well as to identify the smallest number of folds at which the classifier's performance stabilizes. This allows us to estimate the maximum time required, even for high-precision analyses, ensuring efficiency without compromising accuracy.

Initially, 4C data was run through the classifier for all 18 subjects at high fold counts, starting at 250 and increasing up to 3000 in steps of 250 folds. The objective was to identify the cutoff point where performance stabilizes and further increasing the fold count no longer yields benefits. The accuracy metric at this stabilization point will be considered the objective accuracy of the classifier, serving as the benchmark to aim for at lower fold counts as well. Once the

benchmark was established, the data was rerun through the classifier at fold counts ranging from 10 to 100. This approach not only highlights the classifier's performance at low, and therefore practical, fold counts but also helps identify the fold count at which the distribution of partitioning schemes closely resembles the one that produces the benchmark accuracy value. This allows for a more efficient yet accurate analysis by balancing practicality with precision. The same process was then repeated for 2C data. The optimal fold count was determined to be 68 folds for analysis 4C and 69 folds for analysis 2C.

3.3.5 Classifier Performance - Subject Count

Another crucial variable to consider is the subject count. While accuracy is generally expected to improve as the number of subjects increases, provided they have been screened for outliers as shown in subsection 3.3.3, it's important to determine the exact relationship between accuracy and subject count — whether it is linear or more complex. Additionally, identifying if and when performance reaches an asymptote, and at what subject count or chunk count this practically occurs, is essential for optimizing the analysis without unnecessarily increasing the sample size.

A script was developed to automate the classification process for both 4C and 2C analyses across varying subject counts. For 4C, data from 1 to 18 subjects were sequentially fed into the classifier. When more than 2 subjects were involved, the optimal fold count of 68 was maintained. For 1 and 2 subjects, the fold count was set to the maximum possible, which was 4 and 28, respectively.

For 2C, the analysis for a single subject was skipped due to the limitations imposed by having only 2 chunks. The fold count was then set to 4, 15, 28, 45, and 66 for 2, 3, 4, 5, and 6 subjects, respectively, reflecting the maximum feasible number of folds for those subject counts. For all other subject counts, the fold count was standardized at 69.

3.3.6 Ideal Parameters Performance

In the ffa.

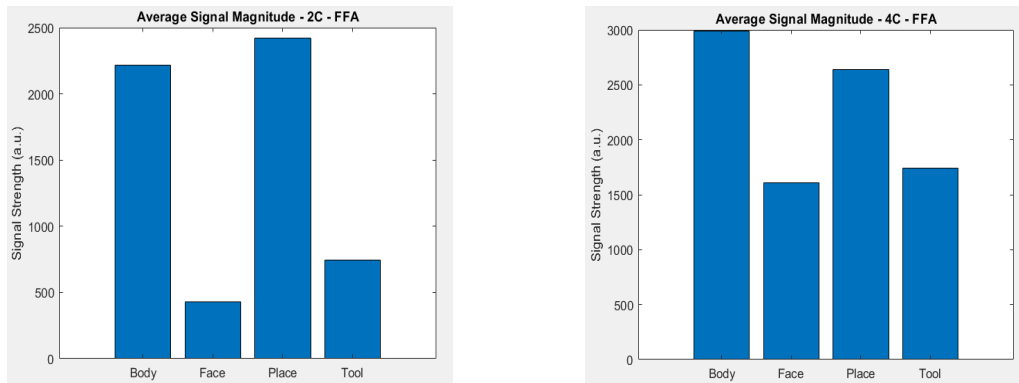
In the ppa.

Chapter 4

Classification Results & Discussion

4.1 Category-Specific Baseline Brain Activation (*UPA*) - Results

The average signal for faces in the FFA is unexpectedly low (see Figure 4.1). However, this does not compromise the efficacy of MVPA, as successful classification of category-specific signals relies on their patterns' distinctiveness from other signals, regardless of whether this distinction is due to signal strength or relative weakness. Nevertheless, this finding warrants further investigation.



(a) Average Magnitude of Brain Activation in the FFA Across Different Stimulus Categories in the 2C Analysis. (b) Average Magnitude of Brain Activation in the FFA Across Different Stimulus Categories in the 4C Analysis.

Figure 4.1: Bar Plots Showing the Mean Activation for Each Stimulus Category Across the FFA.

Examining the WM task battery from which the data was derived, we observe that Faces were presented immediately after Bodies in the first instance and after Places in the second, never directly following a fixation phase. This sequence likely resulted in residual signals from the preceding stimulus categories, which could explain the magnitude observed for Bodies and Places. However, this does not account for the higher magnitude of Tools, which, theoretically, should not surpass that of Faces. A closer examination of the more central portion of the FFA (see Figure 4.2), where residual overlap from other sources is minimized, reveals the expected signal profile: Faces show the highest activation magnitude, with Tools displaying roughly the same relative amplitude. This observation supports the earlier hypothesis and confirms that MVPA can proceed using the initial, full FFA mask.

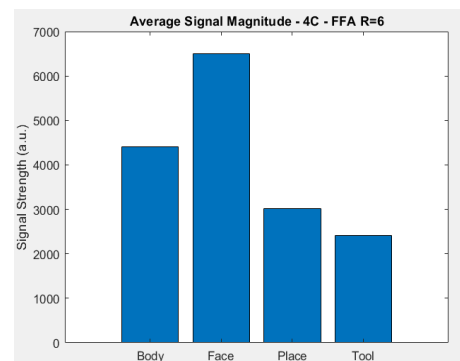
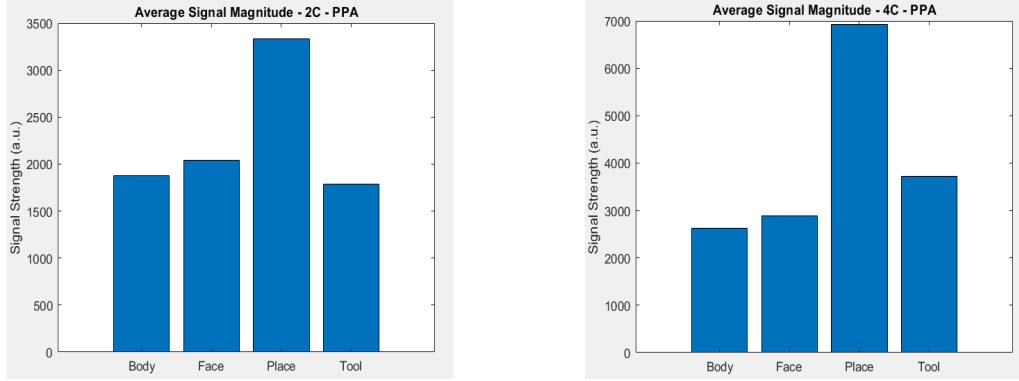


Figure 4.2: Bar Plots Showing the Mean Activation for Each Stimulus Category Across the FFA When Mask Radius is 6.

In contrast, the signal in the PPA is significantly higher for places than other stimuli (see Figure 4.3) throughout the whole region. The category-specific signals also tend to be ranked according to the proximity of their corresponding areas to the PPA, suggesting that the differences in baseline signal may be due to overlap from place stimuli.



(a) Average Magnitude of Brain Activation in the PPA Across Different Stimulus Categories in the 2C Analysis.. (b) Average Magnitude of Brain Activation in the PPA Across Different Stimulus Categories in the 4C Analysis..

Figure 4.3: Bar Plots Showing the Mean Activation for Each Stimulus Category Across the PPA.

Notably, Places were presented once after a fixation phase and once after Tools, ensuring that the resulting signal is more canonical. As a result, the classifier is likely to perform better for place stimuli, although this will ultimately be confirmed or disproven by MVPA.

4.2 Fusiform Face Area MVPA - Results

These are the classifier's performance results for the Fusiform Face Area (FFA), analyzed across different variables.

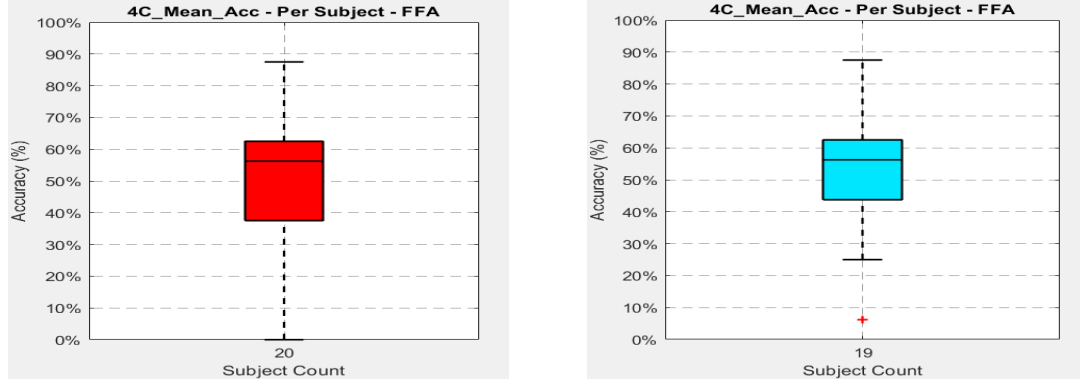
4.2.1 Chunks Per Subject (FFA) - Results

Using 2C data, the classifier achieved an optimal mean accuracy of 70% across 3000 folds in the FFA, while performance with 4C data capped at 61.9%. The distributions of accuracies across folds were tested for normality, and a Lilliefors test confirmed that the data did not follow a normal distribution, with p-values of 10^{-3} for both datasets. Given that the two distributions also differed in variances, as shown by a two-sample F-test with a p-value of $< 10^{-16}$, a Wilcoxon Rank-Sum test was conducted. The discrepancy between means was found to be statistically significant, with a p-value of $< 10^{-16}$, undoubtedly confirming that the different approaches yielded distinct results and that the two analyses should be examined separately.

4.2.2 Outlier Subjects (FFA) - Results

After the classifier ran on each subject's data separately, using the maximum number of folds (4), the mean accuracies for each subject were calculated. As expected, these accuracies were generally lower than those obtained when the classifier was fed larger datasets. When all 20 subjects were included individually, the mean accuracy was 50%, with a median value of 56.3% (see Figure 4.4a). However, two cases stood out immediately: Subject 100408 had a surprising accuracy of 0%, and Subject 116524 showed an accuracy of 6.25%. Given that the classifier completely failed to identify category-specific neural patterns in the first subject's data, it was assumed that the data was faulty for this analysis, and this subject was excluded from further steps. However, no robust reasoning was found to classify the second subject as an outlier, so they were included in the analysis.

Once the outlier was removed, the mean accuracy for analyses involving one subject at a time increased to 52.6%, with the median remaining constant (see Figure 4.4b). Normally, this was



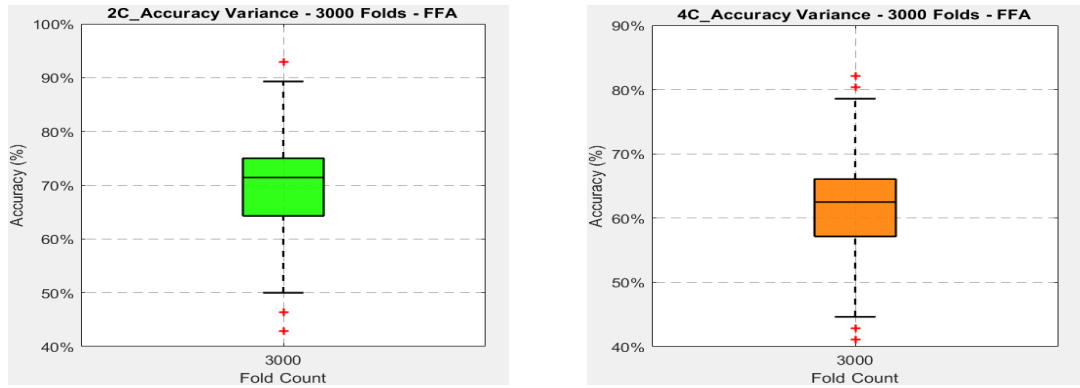
(a) Boxplot Illustrating the Distribution of Initial Accuracy Across Individual Subjects. (b) Boxplot Illustrating Accuracy Variance Across Individual Subjects After Excluding Outliers.

Figure 4.4: Boxplots Generated from the 'Per Subject' Analysis in the FFA.

still lower than the classifier's maximum potential accuracy of 61.9%, which can be attributed to the low fold count used in these analyses. These results clearly indicate that screening for outlier subjects is crucial, as their inclusion can significantly impact the classifier's performance, particularly when working with smaller subject pools.

4.2.3 Fold Count (FFA) - Results

The initial analysis, which focused on high fold counts, showed that accuracy stabilized to the second decimal point by 250 folds for both 4C and 2C analyses. This stability was reflected in the standard deviations of the distributions, which were 0.15% for 4C and 0.17% for 2C. In both cases, accuracy was slightly overestimated in the lower fold range of 250–1000, but eventually plateaued over 2500 folds, reaching 61.9% for 4C and 70% for 2C. These values represent the classifier's true accuracy and serve as the benchmarks to aim for in more practical, lower fold count analyses.



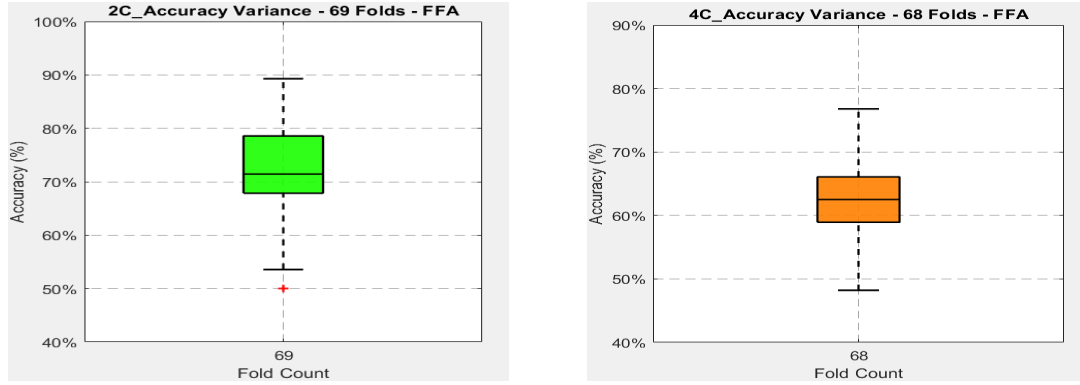
(a) Accuracy Variance Across 3000 Folds for 2C Data.

(b) Accuracy Variance Across 3000 Folds for 4C Data.

Figure 4.5: Boxplots Produced During the 'High Number of Folds' Analysis in the FFA.

Furthermore, Figure 4.5 presents a boxplot for both analyses, illustrating the spread of accuracies across all 3000 folds. This distribution of partitions drives the classifier to its benchmark performance. To establish a practical fold count, the partitioning scheme distribution should mimic the one shown in the boxplot. This rationale led to the optimal practical fold count values being set at 69 for 2C and 68 for 4C.

The boxplots illustrated in Figure 4.6 demonstrate distributions that closely resemble those obtained from the 3000-fold count analysis. These results indicate that the practical fold count approach provides both high accuracy and efficiency, making it a viable alternative for repeated



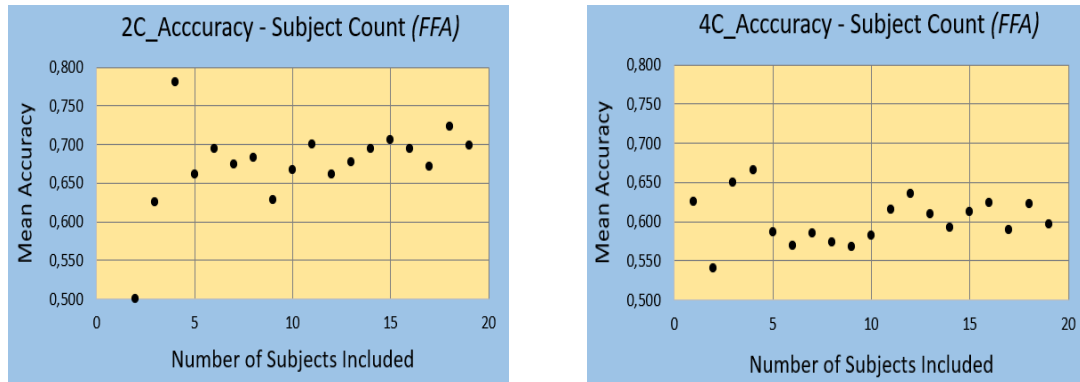
(a) Accuracy Variance Across the Optimal 69 Folds for 2C Data. (b) Accuracy Variance Across the Optimal 68 Folds for 4C Data.

Figure 4.6: Boxplots Produced During the 'Practical Fold Count' Analysis in the FFA.

analyses without compromising on the classifier's performance. The similarity in distributions confirms that reducing the number of folds to a more manageable level does not significantly affect the accuracy of the results.

4.2.4 Subject Count (FFA) - Results

In the context of the 2C analysis, Figure 4.7a shows that with just 2 subjects included, the classifier is already performing at a 50% success rate. As more subjects are added, accuracy naturally increases, oscillating within the 65-70% range, and eventually approaches the classifier's true potential accuracy of 70% with 19 subjects included. The only truly irregular data point occurs at 4 subjects, where the classifier achieves a 78.1% success rate. This anomaly can be attributed to the low number of data points in the analysis at this stage, combined with the necessarily low fold counts used in low subject counts analyses, and does not reflect a realistic performance for the classifier.



(a) Accuracy Variance Across Different Subject Counts for 2C Data. (b) Accuracy Variance Across Different Subject Counts for 4C Data.

Figure 4.7: Data Produced During the 'Subject Count' Analysis in the FFA.

The same behavior is observed for the 4C analysis (see Figure 4.7b). The overly high accuracy pattern at 3 and 4 subjects is repeated, further supporting the idea that brain activation patterns and partitioning schemes at this stage are overly favorable for the classifier. Additionally, another irregular point is observed at a subject count of 1, which was not feasible in the previous analysis. In this case, the fold count is only 4, and the potential performance outcomes are too limited to be truly representative. Therefore, interpreting the data at such low subject counts holds little value.

In both cases, accuracy appears to reach realistic values with at least 5 subjects, showing 66.1% compared to the optimal 69.9% for the 2C analysis and 58.7% compared to the optimal 59.7% for the 4C analysis.

The reasons behind this behavior of the classifier can only be speculated, as the baseline signal appears irregular (see Figure 4.1). A likely explanation is that the rapid stabilization of the classifier's accuracy is not so much a positive sign, as it indicates not that the classifier achieves high success rates at low subject counts but instead that it fails to increase success rate with additional data points. This could be due to the mixed nature of the baseline signal resulting in the disparity among stimuli categories being potentially, yet unpredictably, extenuated as more subjects are included in the analysis.

4.3 Parahippocampal Place Area MVPA - Results

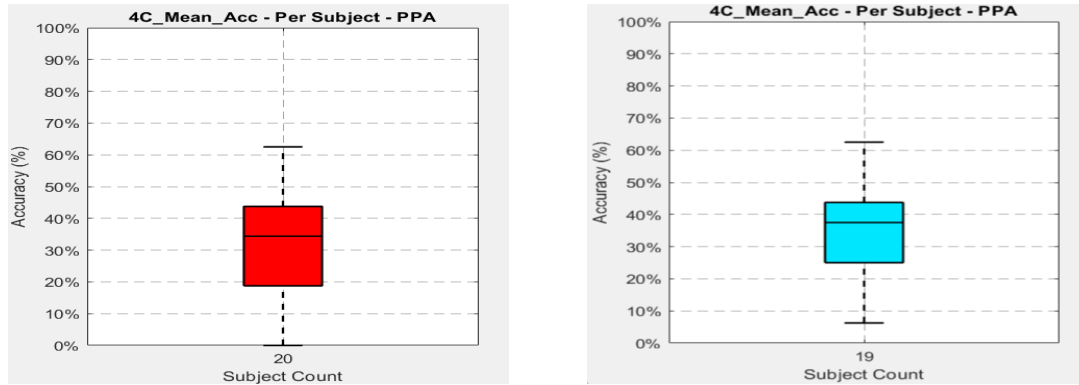
These are the classifier's performance results for the Parahippocampal Place Area (PPA), analyzed across different variables.

4.3.1 Chunks per Subject (PPA) - Results

In the analysis involving 3000 folds in the PPA, the classifier achieved 66.4% accuracy using 2C data and 50.6% with 4C data, highlighting an even larger gap between the two approaches than in the FFA. A Lilliefors test rejected the null hypothesis of normality for both datasets, with p-values of 10^{-3} . The variance between the two datasets was also significantly different, as confirmed by a two-sample F-test with a p-value of $< 10^{-16}$. Finally, the Wilcoxon Rank-Sum test returned a p-value of absolute zero, indicating that it was too low for MATLAB to compute a precise result. This confirms that the two distributions differ significantly and should be investigated separately.

4.3.2 Outlier Subjects (PPA) - Results

In this case individual accuracy scores were far lower than the classifier's optimal performance, with only three out of twenty cases surpassing it, as indicated by the overall mean accuracy of 32.5% when all subjects were included with a median of 34.4% (see Figure 4.8a).



(a) Boxplot Illustrating the Distribution of Initial Accuracy Across Individual Subjects.

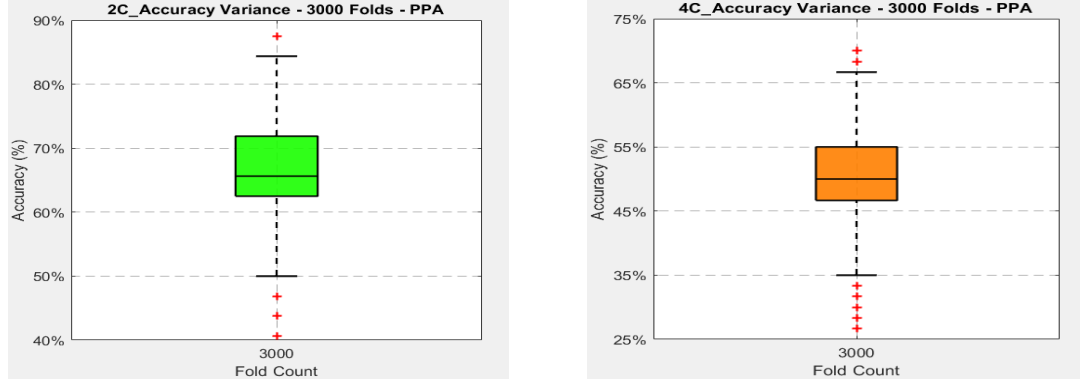
(b) Boxplot Illustrating Accuracy Variance Across Individual Subjects After Excluding Outliers.

Figure 4.8: Boxplots Generated from the 'Per Subject' Analysis in the PPA.

The same Subject 100408 produced an accuracy of 0% again, further enhancing the notion that the specific subject's data potentially includes artifacts or irregularities. Once the outlier subject was excluded, mean accuracy rose to 34.2% with a median of 37.5% (see Figure 4.8b).

4.3.3 Fold Count (PPA) - Results

In both high fold count analyses, accuracy again stabilized to the second decimal point by 250 folds. In the 4C analysis, there was also stabilization to the third decimal point by 750 folds, with standard deviations of 0.12% and 0.07%, for 2C and 4C respectively. In the 2C case, accuracy at low fold counts was slightly lower than the final accuracy ultimately achieved by 2250 folds, which was 66.4%, while with 4C data, accuracy remained practically stable throughout, at 50.6%.

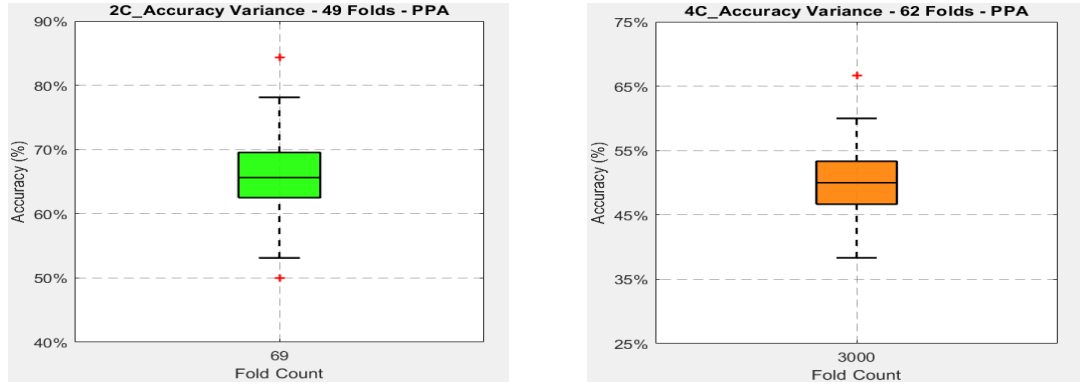


(a) Accuracy Variance Across 3000 Folds for 2C Data.

(b) Accuracy Variance Across 3000 Folds for 4C Data.

Figure 4.9: Boxplots Produced During the 'High Number of Folds' Analysis in the PPA.

Figure 4.9 showcases the spread of accuracies across all 3000 folds for both analyses, indicating the distribution that should be sought after at low fold counts as well. With these in mind, the optimal practical fold count for 2C was set at 49 and for 4C at 62.



(a) Accuracy Variance Across the Optimal 49 Folds for 2C Data.

(b) Accuracy Variance Across the Optimal 62 Folds for 4C Data.

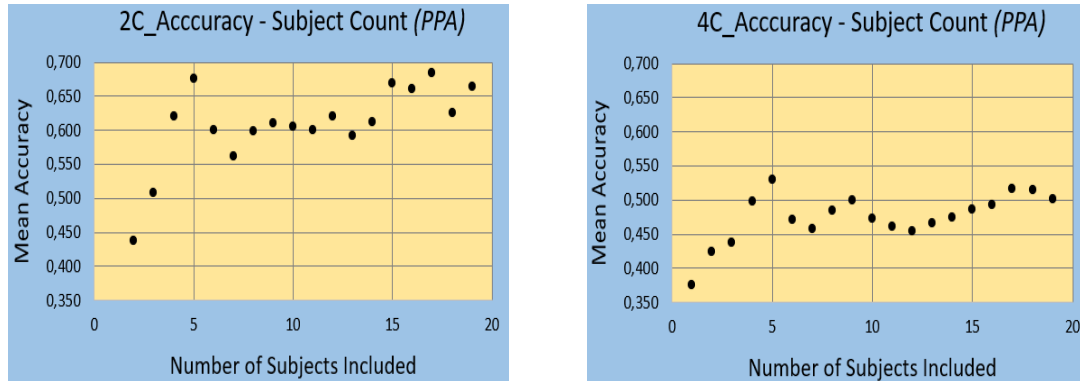
Figure 4.10: Boxplots Produced During the 'Practical Fold Count' Analysis in the PPA.

The accuracy distributions corresponding to the optimal practical fold counts are displayed in Figure 4.10. These distributions mirror those obtained from the 3000-fold count analyses, confirming that the classifier's true accuracy can be attained at lower, more practical fold counts as well.

4.3.4 Subject Count (PPA) - Results

In the 2C analysis (see Figure 4.11a), the classifier begins to perform consistently at around 60% accuracy once more than 6 subjects are included, gradually increasing to 66.8% at 15 subjects and then continuing to oscillate around the final value of 66.4%. At lower subject counts, performance improves rapidly in a linear fashion as more subjects are added, with the only

anomaly occurring at 5 subjects, where a notably precise accuracy of 67.5% is achieved. This subject count could be leveraged for extremely fast, efficient, and relatively accurate analyses, requiring manipulation of just 20 patterns in total.



(a) Accuracy Variance Across Different Subject Counts for 2C Data. (b) Accuracy Variance Across Different Subject Counts for 4C Data.

Figure 4.11: Data Produced During the 'Subject Count' Analysis in the PPA.

A similar pattern is observed in 4C data (see Figure 4.11b), though in an even more stable manner, with smaller deviations from the mean. The same irregularity at 5 subjects is evident, where accuracy peaks at 52.9%. Stabilization initially occurs around a low point of 47% until 14 subjects, after which accuracy slightly oscillates around the final accuracy of 50.1%.

For MVPA in the PPA, classifier performance follows a more typical pattern, improving as the number of subjects and data points increases. Performance appears to plateau after about 15 subjects, with the potential for even higher accuracy as more data is included. This can be attributed to the consistent magnitude of brain activation in the PPA (as shown in Figure 4.3), where the signal for places is significantly higher than for other stimuli. This difference becomes more pronounced with the inclusion of additional subjects and data points, enhancing the classifier's ability to distinguish and accurately classify place-related signals. This effect is even more pronounced in the 4C case, where the disparity between places and other stimuli categories is greater, leading to fewer fluctuations and a more predictable improvement in the classifier's success rate with added data.

4.4 Classification Ideal Parameters

Below is a summary of the variable sets used by the classifier across different functions.

4.4.1 Classifier Maximum Accuracy - Results

The highest classifier performance, 70%, was achieved in the 2C analysis for the FFA, using 3000 folds and 19 subjects, with a completion time of 114.1second. Similarly, with the maximum values of 3000 folds and 19 subjects, the 2C analysis in the PPA achieved a 66.4% success rate in 117.6second.

Interestingly, the maximum accuracy was not obtained with the largest datasets but rather from the analysis that combined 2-Back and 0-Back signals for each stimulus category.

4.4.2 Classifier Maximum Efficiency - Results

In the FFA 2C analysis with only 4 subjects and the maximum possible 28 folds, the process completes in just 1.2second, achieving an accuracy of 78.1%. As for the PPA, in the 2C analysis using 5 subjects and 45 folds, the classifier reaches a success rate of 67.5% in just 1.4second.

While these results cannot be broadly generated with larger datasets, they provide valuable insight into the classifier's potential performance when the data is meticulously screened for artifacts and signals from different stimulus categories are distinctly robust.

4.4.3 Classifier Maximum Practicality - Results

In terms of combining efficiency, precision, and reliability, the 2C analysis with 11 subjects and 69 folds achieves 70% accuracy in just 2.6second for the FFA. This matches the success rate of the exhaustive 3000-fold analysis but accomplishes it in a fraction of the time, while also being based on a sufficiently large dataset to ensure reproducible results. In the PPA, analyzing 2C data from 15 subjects at 49 folds yields a classifier accuracy of 66.8% in 2.9second. The success pattern is similar to that observed for the FFA, although in this case, the data reduction compared to the maximum accuracy analysis was less severe.

These settings should form the basis for the bulk of the analyses, as increasing the magnitude of variables would only demand more computational power and time without offering significant additional benefits.

Chapter 5

Conclusions

Significant progress has been made in brain functional mapping over the past few decades. This thesis has shown the feasibility and efficiency of using MVPA in both the FFA and PPA to decode category-specific neural patterns. As more discoveries link specific brain functions to distinct regions, the methodology presented here offers a framework that can be adapted to a wide range of research questions, both within and beyond the realm of visual processing. The thorough analysis of baseline signals, which integrates traditional univariate methods with advanced multivariate techniques, sets a standard for future research. It also lays the groundwork for the development of more sophisticated tools, enhancing both the quality of results and the efficiency of resource use in the development process.

This research also offers practical implications for the development of more efficient and reliable brain-computer interfaces Brain-Computer Interface (BCIs). The findings demonstrate that accurate neural decoding can be achieved with a reduced number of folds and subjects, significantly lowering the computational cost and time required. This is particularly relevant for clinical applications, where quick and accurate neural decoding could enhance the effectiveness of neurofeedback and other therapeutic interventions.

Looking ahead, future research should explore several avenues to build upon and refine the findings of this study. First, utilizing data from large-scale functional mapping projects, similar in scope to the HCP, could significantly enhance the generalizability, reliability, and statistical power of the results. Additionally, longitudinal studies would be valuable in examining how neural representations evolve over time or with training, offering insights into the plasticity of neural coding.

Another promising direction is to apply MVPA to other brain regions involved in visual processing, such as the OFA and the LOC. Expanding the analysis to these areas could provide a more comprehensive understanding of the neural mechanisms underlying face and place recognition, potentially revealing the hierarchical processing stages across different cortical regions.

Lastly, integrating MVPA with other neuroimaging techniques like EEG or MEG could shed light on the temporal dynamics of category-specific processing. This multimodal approach would bridge the gap between the high spatial resolution of fMRI and the superior temporal resolution of EEG/MEG, offering a more complete and nuanced picture of neural processing.

Despite the promising results, this study is not without its limitations. A notable constraint is the relatively small sample size, which may impact the statistical power and generalizability of the findings. Additionally, the study primarily focused on two specific brain regions, the FFA and PPA. While these areas are key to face and place recognition, and were chosen due to the strong established connections between them and their associated functions, other relevant brain areas were not explored. This narrow focus could limit the broader applicability of the MVPA techniques and the generalization of these classification methods to more complex cognitive processes.

Finally, the study's reliance on data from the HCP may introduce some bias, as this dataset is pre-processed and may not fully represent the variability and complexity of raw fMRI data. Future studies should aim to validate these findings using raw, unprocessed data to ensure the robustness of the conclusions.

In conclusion, this thesis not only advances our understanding of the neural mechanisms underlying category-specific visual processing but also lays the groundwork for future research that could lead to significant developments in both theoretical and applied neuroscience.

Glossary

2C	The FEAT analysis that produced 2 chunks per subject, with a total of 40 chunks.
4C	The FEAT analysis that produced 4 chunks per subject, with a total of 80 chunks.
blob cells	V1 cells that resemble kLGN neurons. They are monocular, color sensitive, characterized by small, concentric receptive fields and are found in clusters, hence the name.
connectomics	The production and study of connectomes: comprehensive maps of connections within an organism's nervous system.
flip angle	The amount of rotation that net magnetization experiences during application of a RF pulse.
gyromagnetic ratio	The gyromagnetic ratio, a constant specific to each different nucleus.
interblob cells	V1 cells, the majority of which are binocular, not color sensitive, characterized by elongated receptive fields, exhibit ocular dominance and orientation specificity, while they are found around the clusters of V1 blob cells.
Time of Echo	The time between the delivery of the RF pulse and the receipt of the echo signal.
TR	The amount of time that passes between consecutive acquired brain volumes.
V1	Visual area V1, the striate cortex or primary visual cortex.

V2	Visual area V2, or secondary visual cortex, also called prestriate cortex.
V3	Visual area V3, which communicates directly with the respective dorsal and ventral subsystems of V2. It is less well-defined compared to other areas of the visual cortex.
V4	Visual area V4, a mid-tier cortical area in the ventral visual pathway.

Acronyms

ASL	Arterial Spin Labeling
BCI	Brain-Computer Interface
BOLD	Blood-Oxygen-Level-Dependent
CBF	Cerebral Blood Flow
COPE	contrast of explanatory variables
CSF	Cerebrospinal Fluid
dMRI	diffusion imaging
DZ	dizygotic
EBA	Extrastriate Body Area
EEG	Electroencephalography
EV	explanatory variable
FBA	Fusiform Body Area
FEAT	FMRIB's Expert Analysis Tool
FFA	Fusiform Face Area
FG	Fusiform Gyrus
fMRI	Functional Magnetic Resonance Imaging
fSTS	Superior Temporal Sulcus
GLM	General Linear Model
Hb	hemoglobin
HbO	Oxyhemoglobin
HbR	deoxyhemoglobin
HbT	total hemoglobin
HCP	Human Connectome Project
HRF	Hemodynamic Response Function
ICA	Independent Component Analysis
IOG	Inferior Occipital Gyrus
IQ	intelligence quotient
IT	Inferior Temporal cortex
ITI	inter-task interval
LGN	Lateral Geniculate Nucleus
LOC	Lateral Occipital Cortex
LOS	Lateral Occipital Sulcus
LR	Left to Right
MEG	Magnetoencephalogram

MOG	Middle Occipital Gyrus
MR	Magnetic Resonance
MRI	Magnetic Resonance Imaging
MT	Middle Temporal visual area
MVPA	Multi-Variate Pattern Analysis
MZ	monozygotic
NIFTI	Neuroimaging Informatics Technology Initiative
NIH	National Institutes of Health
NIRS	Near Infrared Spectroscopy
NMR	Nuclear Magnetic Resonance
OEF	Oxygen Extraction Fraction
OFA	Occipital Face Area
PCA	Principal Component Analysis
PDF	probability density function
PET	Positron Emission Tomography
PPA	Parahippocampal Place Area
r-fMRI	resting-state fMRI
RF	radio frequency
RL	Right to Left
ROI	Region of Interest
ROIs	Regions of Interest
SLU	Saint Louis University
SVM	Support Vector Machine
SVMs	Support Vector Machines
t-fMRI	task-evoked fMRI
T-MEG	task-evoked MEG
T1w	T1-weighted
T2w	T2-weighted
UMinn	University of Minnesota
UPA	Univariate Pattern Analysis
USA	United States of America
WashU	Washington University
WM	Working Memory

Bibliography

- [1] *Visual processing: Cortical pathways (section 2, chapter 15) neuroscience online: An electronic textbook for the neurosciences | department of neurobiology and anatomy - the university of texas medical school at houston.* [Online]. Available: <https://nba.uth.tmc.edu/neuroscience/m/s2/chapter15.html>.
- [2] M. Gupta, A. C. Ireland, and B. Bordoni, *Neuroanatomy, Visual Pathway*. StatPearls Publishing, Dec. 2022.
- [3] M. Mishkin, L. G. Ungerleider, and K. A. Macko, "Object vision and spatial vision: Two cortical pathways," *Trends in Neurosciences*, vol. 6, pp. 414–417, C Jan. 1983, issn: 0166-2236. doi: [10.1016/0166-2236\(83\)90190-X](https://doi.org/10.1016/0166-2236(83)90190-X).
- [4] J. V. Haxby, C. L. Grady, B. Horwitz, *et al.*, "Dissociation of object and spatial visual processing pathways in human extrastriate cortex.," *Proceedings of the National Academy of Sciences*, vol. 88, pp. 1621–1625, 5 Mar. 1991, issn: 00278424. doi: [10.1073/PNAS.88.5.1621](https://doi.org/10.1073/PNAS.88.5.1621). [Online]. Available: <https://www.pnas.org/doi/abs/10.1073/pnas.88.5.1621>.
- [5] J. Sergent, S. Ohta, and B. Macdonald, "Functional neuroanatomy of face and object processing: A positron emission tomography study," *Brain*, vol. 115, pp. 15–36, 1 Feb. 1992, issn: 0006-8950. doi: [10.1093/BRAIN/115.1.15](https://doi.org/10.1093/BRAIN/115.1.15). [Online]. Available: <https://dx.doi.org/10.1093/brain/115.1.15>.
- [6] A. Puce, T. Allison, M. Asgari, J. C. Gore, and G. McCarthy, "Differential sensitivity of human visual cortex to faces, letterstrings, and textures: A functional magnetic resonance imaging study," *The Journal of Neuroscience*, vol. 16, p. 5205, 16 Aug. 1996, issn: 02706474. doi: [10.1523/JNEUROSCI.16-16-05205.1996](https://doi.org/10.1523/JNEUROSCI.16-16-05205.1996). [Online]. Available: [/pmc/articles/PMC6579313/](https://www.ncbi.nlm.nih.gov/pmc/articles/PMC6579313/) <https://www.ncbi.nlm.nih.gov/pmc/articles/PMC6579313/?report=abstract%20https://www.ncbi.nlm.nih.gov/pmc/articles/PMC6579313/>.
- [7] G. McCarthy, M. Luby, J. Gore, and P. Goldman-Rakic, "Infrequent events transiently activate human prefrontal and parietal cortex as measured by functional mri," *Journal of neurophysiology*, vol. 77, pp. 1630–1634, 3 1997, issn: 0022-3077. doi: [10.1152/JN.1997.77.3.1630](https://doi.org/10.1152/JN.1997.77.3.1630). [Online]. Available: <https://pubmed.ncbi.nlm.nih.gov/9084626/>.
- [8] N. Kanwisher, J. McDermott, and M. M. Chun, "The fusiform face area: A module in human extrastriate cortex specialized for face perception," *The Journal of Neuroscience*, vol. 17, p. 4302, 11 Jun. 1997, issn: 02706474. doi: [10.1523/JNEUROSCI.17-11-04302.1997](https://doi.org/10.1523/JNEUROSCI.17-11-04302.1997). [Online]. Available: [/pmc/articles/PMC6573547/](https://www.ncbi.nlm.nih.gov/pmc/articles/PMC6573547/) <https://www.ncbi.nlm.nih.gov/pmc/articles/PMC6573547/?report=abstract%20https://www.ncbi.nlm.nih.gov/pmc/articles/PMC6573547/>.
- [9] N. Kanwisher and G. Yovel, "The fusiform face area: A cortical region specialized for the perception of faces," *Philosophical Transactions of the Royal Society B: Biological Sciences*, vol. 361, p. 2109, 1476 Dec. 2006, issn: 09628436. doi: [10.1098/RSTB.2006.1934](https://doi.org/10.1098/RSTB.2006.1934). [Online]. Available: [/pmc/articles/PMC1857737/](https://www.ncbi.nlm.nih.gov/pmc/articles/PMC1857737/) <https://www.ncbi.nlm.nih.gov/pmc/articles/PMC1857737/?report=abstract%20https://www.ncbi.nlm.nih.gov/pmc/articles/PMC1857737/>.
- [10] R. Epstein and N. Kanwisher, "A cortical representation of the local visual environment," *Nature* 1998 392:6676, vol. 392, pp. 598–601, 6676 Apr. 1998, issn: 1476-4687. doi: [10.1038/33402](https://doi.org/10.1038/33402). [Online]. Available: <https://www.nature.com/articles/33402>.

- [11] R. Epstein, A. Harris, D. Stanley, and N. Kanwisher, "The parahippocampal place area: Recognition, navigation, or encoding?" *Neuron*, vol. 23, pp. 115–125, 1 May 1999, issn: 0896-6273. doi: [10.1016/S0896-6273\(00\)80758-8](https://doi.org/10.1016/S0896-6273(00)80758-8).
- [12] R. Epstein, K. S. Graham, and P. E. Downing, "Viewpoint-specific scene representations in human parahippocampal cortex," *Neuron*, vol. 37, pp. 865–876, 5 Mar. 2003, issn: 08966273. doi: [10.1016/S0896-6273\(03\)00117-X](https://doi.org/10.1016/S0896-6273(03)00117-X). [Online]. Available: <https://pubmed.ncbi.nlm.nih.gov/12628176/>.
- [13] S. Park and M. M. Chun, "Different roles of the parahippocampal place area (ppa) and retrosplenial cortex (rsc) in panoramic scene perception," *NeuroImage*, vol. 47, p. 1747, 4 Oct. 2009, issn: 10538119. doi: [10.1016/J.NEUROIMAGE.2009.04.058](https://doi.org/10.1016/J.NEUROIMAGE.2009.04.058). [Online]. Available: [/pmc/articles/PMC2753672/%20/pmc/articles/PMC2753672/?report=abstract%20https://www.ncbi.nlm.nih.gov/pmc/articles/PMC2753672/](https://pubmed.ncbi.nlm.nih.gov/PMC2753672/).
- [14] R. Malach, J. B. Reppas, R. R. Benson, *et al.*, "Object-related activity revealed by functional magnetic resonance imaging in human occipital cortex.," *Proceedings of the National Academy of Sciences*, vol. 92, pp. 8135–8139, 18 Aug. 1995, issn: 00278424. doi: [10.1073/PNAS.92.18.8135](https://doi.org/10.1073/PNAS.92.18.8135). [Online]. Available: <https://www.pnas.org/doi/abs/10.1073/pnas.92.18.8135>.
- [15] N. Kanwisher, M. M. Chun, J. McDermott, and P. J. Ledden, "Functional imaging of human visual recognition," *Cognitive Brain Research*, vol. 5, pp. 55–67, 1-2 Dec. 1996, issn: 0926-6410. doi: [10.1016/S0926-6410\(96\)00041-9](https://doi.org/10.1016/S0926-6410(96)00041-9).
- [16] K. Grill-Spector, T. Kushnir, T. Hendler, S. Edelman, Y. Itzhak, and R. Malach, "A sequence of object-processing stages revealed by fmri in the human occipital lobe," *Human Brain Mapping*, vol. 6, no. 4, pp. 316–328, 1998, issn: 1065-9471. doi: [10.1002/\(sici\)1097-0193\(1998\)6:4<316::aid-hbm9>3.0.co;2-6](https://doi.org/10.1002/(sici)1097-0193(1998)6:4<316::aid-hbm9>3.0.co;2-6). [Online]. Available: [http://dx.doi.org/10.1002/\(SICI\)1097-0193\(1998\)6:4%3C316::AID-HBM9%3E3.0.CO;2-6](http://dx.doi.org/10.1002/(SICI)1097-0193(1998)6:4%3C316::AID-HBM9%3E3.0.CO;2-6).
- [17] S. Murtha, H. Chertkow, M. Beauregard, and A. Evans, "The neural substrate of picture naming," *Journal of Cognitive Neuroscience*, vol. 11, pp. 399–423, 4 Jul. 1999, issn: 0898-929X. doi: [10.1162/089892999563508](https://doi.org/10.1162/089892999563508). [Online]. Available: <https://dx.doi.org/10.1162/089892999563508>.
- [18] K. Grill-Spector, Z. Kourtzi, and N. Kanwisher, "The lateral occipital complex and its role in object recognition," *Vision Research*, vol. 41, pp. 1409–1422, 10-11 May 2001, issn: 0042-6989. doi: [10.1016/S0042-6989\(01\)00073-6](https://doi.org/10.1016/S0042-6989(01)00073-6).
- [19] P. E. Downing, Y. Jiang, M. Shuman, and N. Kanwisher, "A cortical area selective for visual processing of the human body," *Science*, vol. 293, pp. 2470–2473, 5539 Sep. 2001, issn: 00368075. doi: [10.1126/SCIENCE.1063414](https://doi.org/10.1126/SCIENCE.1063414). [Online]. Available: <https://www.science.org/doi/10.1126/science.1063414>.
- [20] M. V. Peelen and P. E. Downing, "Selectivity for the human body in the fusiform gyrus," *Journal of Neurophysiology*, vol. 93, pp. 603–608, 1 Jan. 2005, issn: 00223077. doi: [10.1152/JN.00513.2004/ASSET/IMAGES/LARGE/Z9K0010543090003.JPEG](https://doi.org/10.1152/JN.00513.2004/ASSET/IMAGES/LARGE/Z9K0010543090003.JPEG). [Online]. Available: <https://journals.physiology.org/doi/10.1152/jn.00513.2004>.
- [21] M. Spiridon, B. Fischl, and N. Kanwisher, "Location and spatial profile of category-specific regions in human extrastriate cortex," *Human Brain Mapping*, vol. 27, pp. 77–89, 1 Jan. 2006, issn: 10659471. doi: [10.1002/HBM.20169](https://doi.org/10.1002/HBM.20169).
- [22] K. S. Weiner and K. Grill-Spector, "Sparsely-distributed organization of face and limb activations in human ventral temporal cortex," *NeuroImage*, vol. 52, pp. 1559–1573, 4 Oct. 2010, issn: 1053-8119. doi: [10.1016/J.NEUROIMAGE.2010.04.262](https://doi.org/10.1016/J.NEUROIMAGE.2010.04.262).
- [23] L. Amoroso, B. Couto, and A. Ibáñez, "Beyond extrastriate body area (eba) and fusiform body area (fba): Context integration in the meaning of actions," *Frontiers in Human Neuroscience*, vol. 5, p. 13143, Nov. 2011, issn: 16625161. doi: [10.3389/FNHUM.2011.00124/BIBTEX](https://doi.org/10.3389/FNHUM.2011.00124/BIBTEX).

- [24] A. Pann, M. Bonnard, O. Felician, and P. Romaiguère, “The extrastriate body area and identity processing: An fmri guided tms study,” *Physiological Reports*, vol. 9, 8 Apr. 2021, issn: 2051817X. doi: 10.14814/PHY2.14711. [Online]. Available: [/pmc/articles/PMC8090840/%20/pmc/articles/PMC8090840/?report=abstract%20https://www.ncbi.nlm.nih.gov/pmc/articles/PMC8090840/](https://www.ncbi.nlm.nih.gov/pmc/articles/PMC8090840/?report=abstract%20https://www.ncbi.nlm.nih.gov/pmc/articles/PMC8090840/).
- [25] J. C. Taylor, A. J. Wiggett, and P. E. Downing, “Functional mri analysis of body and body part representations in the extrastriate and fusiform body areas,” *Journal of Neurophysiology*, vol. 98, pp. 1626–1633, 3 Sep. 2007, issn: 00223077. doi: 10.1152/JN.00012.2007/ASSET/IMAGES/LARGE/Z9K0090783830004.JPEG. [Online]. Available: <https://journals.physiology.org/doi/10.1152/jn.00012.2007>.
- [26] *The visual centers of the brain | the visionhelp blog*. [Online]. Available: <https://visionhelp.wordpress.com/2018/07/04/the-visual-centers-of-the-brain/>.
- [27] *(pdf) occipital brain damage in visual processing. behavioral and functional (fmri) approaches of cortical reorganization*. [Online]. Available: https://www.researchgate.net/publication/278642708_Occipital_brain_damage_in_visual_processing_Behavioral_and_functional_fMRI_approaches_of_cortical_reorganization.
- [28] *Prosopagnosia | fusiform face area functions and impact*. [Online]. Available: <https://prosopagnosiabytmayo.wordpress.com/>.
- [29] *Prosopagnosia | fusiform face area functions and impact*. [Online]. Available: <https://prosopagnosiabytmayo.wordpress.com/>.
- [30] R. F. Schwarzlose, C. I. Baker, and N. Kanwisher, “Separate face and body selectivity on the fusiform gyrus,” *The Journal of neuroscience : the official journal of the Society for Neuroscience*, vol. 25, pp. 11 055–11 059, 47 Nov. 2005, issn: 1529-2401. doi: 10.1523/JNEUROSCI.2621-05.2005. [Online]. Available: <https://pubmed.ncbi.nlm.nih.gov/16306418/>.
- [31] M. Li, H. Huang, B. Guo, and M. Meng, “Distinct response properties between the ffa to faces and the ppa to houses,” *Brain and Behavior*, vol. 12, e2706, 8 Aug. 2022, issn: 2162-3279. doi: 10.1002/BRB3.2706. [Online]. Available: <https://onlinelibrary.wiley.com/doi/full/10.1002/brb3.2706%20https://onlinelibrary.wiley.com/doi/abs/10.1002/brb3.2706%20https://onlinelibrary.wiley.com/doi/10.1002/brb3.2706>.
- [32] G. XUE, C. CHEN, Z.-L. LU, and Q. DONG, “Brain imaging techniques and their applications in decision-making research,” *Xin li xue bao. Acta psychologica Sinica*, vol. 42, p. 120, 1 Feb. 2010, issn: 0439-755X. doi: 10.3724/SP.J.1041.2010.00120. [Online]. Available: [/pmc/articles/PMC2849100/%20/pmc/articles/PMC2849100/?report=abstract%20https://www.ncbi.nlm.nih.gov/pmc/articles/PMC2849100/](https://www.ncbi.nlm.nih.gov/pmc/articles/PMC2849100/?report=abstract%20https://www.ncbi.nlm.nih.gov/pmc/articles/PMC2849100/).
- [33] R. B. Buxton, “The physics of functional magnetic resonance imaging (fmri),” *Reports on Progress in Physics*, vol. 76, 9 Sep. 2013, issn: 00344885. doi: 10.1088/0034-4885/76/9/096601.
- [34] A. Suriaga, R. M. Tappen, E. R. Aston, L. Chiang-Hanisko, and D. Newman, “The physics of fmri,” *Journal of Nursing Scholarship*, vol. 26, pp. 623–636, 3 May 2009, issn: 15475069. [Online]. Available: <https://www.psychiatrictimes.com/view/physics-fmri>.
- [35] *T1 relaxation - questions and answers in mri*. [Online]. Available: <https://mriquestions.com/what-is-t1.html>.
- [36] J. A. Detre, J. S. Leigh, D. S. Williams, and A. P. Koretsky, “Perfusion imaging,” *Magnetic Resonance in Medicine*, vol. 23, pp. 37–45, 1 Jan. 1992, issn: 1522-2594. doi: 10.1002/MRM.1910230106. [Online]. Available: <https://onlinelibrary.wiley.com/doi/full/10.1002/mrm.1910230106%20https://onlinelibrary.wiley.com/doi/abs/10.1002/mrm.1910230106%20https://onlinelibrary.wiley.com/doi/10.1002/mrm.1910230106>.
- [37] *T2 (spin-spin) relaxation - questions and answers in mri*. [Online]. Available: <https://mriquestions.com/what-is-t2.html>.
- [38] *T2* vs t2 relaxation time - questions and answers in mri*. [Online]. Available: <https://www.mriquestions.com/t2-vs-t2.html>.

- [39] S. G. Kim and S. Ogawa, "Biophysical and physiological origins of blood oxygenation level-dependent fmri signals," *Journal of Cerebral Blood Flow and Metabolism*, vol. 32, pp. 1188–1206, 7 Jul. 2012, issn: 0271678X. doi: [10.1038/JCBFM.2012.23/ASSET/IMAGES/LARGE/10.1038_JCBFM.2012.23-FIG6.JPEG](https://doi.org/10.1038/JCBFM.2012.23/ASSET/IMAGES/LARGE/10.1038_JCBFM.2012.23-FIG6.JPEG). [Online]. Available: <https://journals.sagepub.com/doi/full/10.1038/jcbfm.2012.23>.
- [40] H. Ito, I. Kanno, H. Iida, *et al.*, "Arterial fraction of cerebral blood volume in humans measured by positron emission tomography," *Annals of Nuclear Medicine*, vol. 15, pp. 111–116, 2 2001, issn: 09147187. doi: [10.1007/BF02988600/METRICS](https://doi.org/10.1007/BF02988600/METRICS). [Online]. Available: <https://link.springer.com/article/10.1007/BF02988600>.
- [41] H. An and W. Lin, "Cerebral venous and arterial blood volumes can be estimated separately in humans using magnetic resonance imaging," *Magnetic Resonance in Medicine*, vol. 48, pp. 583–588, 4 Oct. 2002, issn: 1522-2594. doi: [10.1002/MRM.10257](https://doi.org/10.1002/MRM.10257). [Online]. Available: <https://onlinelibrary.wiley.com/doi/full/10.1002/mrm.10257%20https://onlinelibrary.wiley.com/doi/abs/10.1002/mrm.10257%20https://onlinelibrary.wiley.com/doi/10.1002/mrm.10257>.
- [42] H. An and W. Lin, "Cerebral oxygen extraction fraction and cerebral venous blood volume measurements using mri: Effects of magnetic field variation," *Magnetic Resonance in Medicine*, vol. 47, pp. 958–966, 5 May 2002, issn: 1522-2594. doi: [10.1002/MRM.10148](https://doi.org/10.1002/MRM.10148). [Online]. Available: <https://onlinelibrary.wiley.com/doi/full/10.1002/mrm.10148%20https://onlinelibrary.wiley.com/doi/abs/10.1002/mrm.10148%20https://onlinelibrary.wiley.com/doi/10.1002/mrm.10148>.
- [43] *Part 2 – t2 relaxation: Definition, measurement and practical implications! — nanalysis*. [Online]. Available: <https://www.nanalysis.com/nmready-blog/2020/6/1/part-2-t2-relaxation-definition-measurement-and-practical-implications-wps35>.
- [44] S. Mayda, Z. Kandemir, N. Bulut, and S. Maekawa, "Magnetic mechanism for the biological functioning of hemoglobin," *Scientific Reports*, vol. 10, 1 Dec. 2020, issn: 20452322. doi: [10.1038/s41598-020-64364-y](https://doi.org/10.1038/s41598-020-64364-y). [Online]. Available: <https://www.nature.com/articles/s41598-020-64364-y>.
- [45] D. Attwell and C. Iadecola, "The neural basis of functional brain imaging signals," *Trends in neurosciences*, vol. 25, no. 12, pp. 621–625, 2002.
- [46] M. E. Raichle, *Neuroimaging of human brain function*, 1998. [Online]. Available: www.pnas.org.
- [47] E. M. C. Hillman, "Optical brain imaging in vivo: Techniques and applications from animal to man," *Journal of Biomedical Optics*, vol. 12, p. 051402, 5 2007, issn: 10833668. doi: [10.1117/1.2789693](https://doi.org/10.1117/1.2789693).
- [48] E. M. Hillman, *Coupling mechanism and significance of the bold signal: A status report*, 2014. doi: [10.1146/annurev-neuro-071013-014111](https://doi.org/10.1146/annurev-neuro-071013-014111).
- [49] N. K. Logothetis, "Neurovascular uncoupling: Much ado about nothing," *Frontiers in Neuroenergetics*, vol. 2, 2010. doi: [10.3389/fnene.2010.00002](https://doi.org/10.3389/fnene.2010.00002).
- [50] D. C. V. Essen and K. Ugurbil, "The future of the human connectome," *NeuroImage*, vol. 62, pp. 1299–1310, 2 Aug. 2012, issn: 1053-8119. doi: [10.1016/J.NEUROIMAGE.2012.01.032](https://doi.org/10.1016/J.NEUROIMAGE.2012.01.032).
- [51] D. C. V. Essen, K. Ugurbil, E. Auerbach, *et al.*, "The human connectome project: A data acquisition perspective," *NeuroImage*, vol. 62, p. 2222, 4 Oct. 2012, issn: 10538119. doi: [10.1016/J.NEUROIMAGE.2012.02.018](https://doi.org/10.1016/J.NEUROIMAGE.2012.02.018). [Online]. Available: [/pmc/articles/PMC3606888/%20/pmc/articles/PMC3606888/?report=abstract%20https://www.ncbi.nlm.nih.gov/pmc/articles/PMC3606888/](https://pmc/articles/PMC3606888/%20/pmc/articles/PMC3606888/?report=abstract%20https://www.ncbi.nlm.nih.gov/pmc/articles/PMC3606888/).
- [52] C. E. Sartor, K. K. Bucholz, E. C. Nelson, P. A. Madden, M. T. Lynskey, and A. C. Heath, "Reporting bias in the association between age at first alcohol use and heavy episodic drinking," *Alcoholism: Clinical and Experimental Research*, vol. 35, pp. 1418–1425, 8 Aug. 2011, issn: 1530-0277. doi: [10.1111/J.1530-0277.2011.01477.X](https://doi.org/10.1111/J.1530-0277.2011.01477.X). [Online]. Available: <https://onlinelibrary.wiley.com/doi/full/10.1111/j.1530-0277.2011.01477.x%20https://onlinelibrary.wiley.com/doi/abs/10.1111/j.1530-0277.2011.01477.x%20https://onlinelibrary.wiley.com/doi/10.1111/j.1530-0277.2011.01477.x>.

- [53] E. L. Edens, A. L. Glowinski, M. L. Pergadia, C. N. Lessov-Schlaggar, and K. K. Buchholz, "Nicotine addiction in light smoking african american mothers," *Journal of Addiction Medicine*, vol. 4, pp. 55–60, 1 Mar. 2010, issn: 19320620. doi: [10.1097/ADM.0B013E3181AF111E](https://doi.org/10.1097/ADM.0B013E3181AF111E). [Online]. Available: https://journals.lww.com/journaladdictionmedicine/fulltext/2010/03000/nicotine_addiction_in_light_smoking_african.8.aspx.
- [54] D. M. Barch, G. C. Burgess, M. P. Harms, *et al.*, "Function in the human connectome: Task-fMRI and individual differences in behavior," *NeuroImage*, vol. 80, pp. 169–189, Oct. 2013, issn: 1053-8119. doi: [10.1016/J.NEUROIMAGE.2013.05.033](https://doi.org/10.1016/J.NEUROIMAGE.2013.05.033).
- [55] D. S. Bassett, E. T. Bullmore, A. Meyer-Lindenberg, J. A. Apud, D. R. Weinberger, and R. Coppola, "Cognitive fitness of cost-efficient brain functional networks," *Proceedings of the National Academy of Sciences of the United States of America*, vol. 106, pp. 11747–11752, 28 Jul. 2009, issn: 1091-6490. doi: [10.1073/PNAS.0903641106](https://doi.org/10.1073/PNAS.0903641106). [Online]. Available: <https://pubmed.ncbi.nlm.nih.gov/19564605/>.
- [56] M. Song, Y. Zhou, J. Li, *et al.*, "Brain spontaneous functional connectivity and intelligence," *NeuroImage*, vol. 41, pp. 1168–1176, 3 Jul. 2008, issn: 1053-8119. doi: [10.1016/J.NEUROIMAGE.2008.02.036](https://doi.org/10.1016/J.NEUROIMAGE.2008.02.036). [Online]. Available: <https://pubmed.ncbi.nlm.nih.gov/18434203/>.
- [57] M. P. V. D. Heuvel, C. J. Stam, R. S. Kahn, and H. E. H. Pol, "Efficiency of functional brain networks and intellectual performance," *The Journal of neuroscience : the official journal of the Society for Neuroscience*, vol. 29, pp. 7619–7624, 23 Jun. 2009, issn: 1529-2401. doi: [10.1523/JNEUROSCI.1443-09.2009](https://doi.org/10.1523/JNEUROSCI.1443-09.2009). [Online]. Available: <https://pubmed.ncbi.nlm.nih.gov/19515930/>.
- [58] Y. Li, Y. Liu, J. Li, *et al.*, "Brain anatomical network and intelligence," *PLoS computational biology*, vol. 5, 5 2009, issn: 1553-7358. doi: [10.1371/JOURNAL.PCBI.1000395](https://doi.org/10.1371/JOURNAL.PCBI.1000395). [Online]. Available: <https://pubmed.ncbi.nlm.nih.gov/19492086/>.
- [59] M. W. Cole, T. Yarkoni, G. Repovš, A. Anticevic, and T. S. Braver, "Global connectivity of prefrontal cortex predicts cognitive control and intelligence," *The Journal of neuroscience : the official journal of the Society for Neuroscience*, vol. 32, pp. 8988–8999, 26 Jun. 2012, issn: 1529-2401. doi: [10.1523/JNEUROSCI.0536-12.2012](https://doi.org/10.1523/JNEUROSCI.0536-12.2012). [Online]. Available: <https://pubmed.ncbi.nlm.nih.gov/22745498/>.
- [60] D. A. Fair, N. U. Dosenbach, J. A. Church, *et al.*, "Development of distinct control networks through segregation and integration," *Proceedings of the National Academy of Sciences of the United States of America*, vol. 104, pp. 13507–13512, 33 Aug. 2007, issn: 0027-8424. doi: [10.1073/PNAS.0705843104](https://doi.org/10.1073/PNAS.0705843104). [Online]. Available: <https://pubmed.ncbi.nlm.nih.gov/17679691/>.
- [61] D. A. Fair, A. L. Cohen, J. D. Power, *et al.*, "Functional brain networks develop from a "local to distributed" organization," *PLoS computational biology*, vol. 5, 5 2009, issn: 1553-7358. doi: [10.1371/JOURNAL.PCBI.1000381](https://doi.org/10.1371/JOURNAL.PCBI.1000381). [Online]. Available: <https://pubmed.ncbi.nlm.nih.gov/19412534/>.
- [62] K. Hwang, M. N. Hallquist, and B. Luna, "The development of hub architecture in the human functional brain network," *Cerebral cortex (New York, N.Y. : 1991)*, vol. 23, pp. 2380–2393, 10 Oct. 2013, issn: 1460-2199. doi: [10.1093/CERCOR/BHS227](https://doi.org/10.1093/CERCOR/BHS227). [Online]. Available: <https://pubmed.ncbi.nlm.nih.gov/22875861/>.
- [63] D. Imperati, S. Colcombe, C. Kelly, *et al.*, "Differential development of human brain white matter tracts," *PloS one*, vol. 6, 8 2011, issn: 1932-6203. doi: [10.1371/JOURNAL.PONE.0023437](https://doi.org/10.1371/JOURNAL.PONE.0023437). [Online]. Available: <https://pubmed.ncbi.nlm.nih.gov/21909351/>.
- [64] M. C. Stevens, P. Skudlarski, G. D. Pearlson, and V. D. Calhoun, "Age-related cognitive gains are mediated by the effects of white matter development on brain network integration," *NeuroImage*, vol. 48, pp. 738–746, 4 Dec. 2009, issn: 1095-9572. doi: [10.1016/J.NEUROIMAGE.2009.06.065](https://doi.org/10.1016/J.NEUROIMAGE.2009.06.065). [Online]. Available: <https://pubmed.ncbi.nlm.nih.gov/19577651/>.

- [65] K. Supekar, M. Musen, and V. Menon, "Development of large-scale functional brain networks in children," *PLoS biology*, vol. 7, 7 Jul. 2009, issn: 1545-7885. doi: [10.1371/JOURNAL.PBIO.1000157](https://doi.org/10.1371/JOURNAL.PBIO.1000157). [Online]. Available: <https://pubmed.ncbi.nlm.nih.gov/19621066/>.
- [66] X. N. Zuo, C. Kelly, A. D. Martino, *et al.*, "Growing together and growing apart: Regional and sex differences in the lifespan developmental trajectories of functional homotopy," *The Journal of neuroscience : the official journal of the Society for Neuroscience*, vol. 30, pp. 15 034–15 043, 45 Nov. 2010, issn: 1529-2401. doi: [10.1523/JNEUROSCI.2612-10.2010](https://doi.org/10.1523/JNEUROSCI.2612-10.2010). [Online]. Available: <https://pubmed.ncbi.nlm.nih.gov/21068309/>.
- [67] *Home - nih toolbox*. [Online]. Available: <https://nihtoolbox.org/>.
- [68] J. W. Dalley, A. C. Mar, D. Economidou, and T. W. Robbins, "Neurobehavioral mechanisms of impulsivity: Fronto-striatal systems and functional neurochemistry," *Pharmacology, biochemistry, and behavior*, vol. 90, pp. 250–260, 2 Aug. 2008, issn: 0091-3057. doi: [10.1016/J.PBB.2007.12.021](https://doi.org/10.1016/J.PBB.2007.12.021). [Online]. Available: <https://pubmed.ncbi.nlm.nih.gov/18272211/>.
- [69] N. A. Shamosh, C. G. DeYoung, A. E. Green, *et al.*, "Individual differences in delay discounting: Relation to intelligence, working memory, and anterior prefrontal cortex," *Psychological science*, vol. 19, pp. 904–911, 9 Sep. 2008, issn: 1467-9280. doi: [10.1111/J.1467-9280.2008.02175.X](https://doi.org/10.1111/J.1467-9280.2008.02175.X). [Online]. Available: <https://pubmed.ncbi.nlm.nih.gov/18947356/>.
- [70] G. C. Burgess, J. R. Gray, A. R. Conway, and T. S. Braver, "Neural mechanisms of interference control underlie the relationship between fluid intelligence and working memory span," *Journal of experimental psychology. General*, vol. 140, pp. 674–692, 4 Nov. 2011, issn: 1939-2222. doi: [10.1037/A0024695](https://doi.org/10.1037/A0024695). [Online]. Available: <https://pubmed.ncbi.nlm.nih.gov/21787103/>.
- [71] *Connectome - hcp 3t task fmri protocol overview*. [Online]. Available: <https://www.humanconnectome.org/hcp-protocols-ya-task-fmri>.
- [72] C. G. Habeck, "Basics of multivariate analysis in neuroimaging data," *Journal of Visualized Experiments : JoVE*, p. 1988, 41 2010, issn: 1940087X. doi: [10.3791/1988](https://doi.org/10.3791/1988). [Online]. Available: [/pmc/articles/PMC3074457/](https://www.ncbi.nlm.nih.gov/pmc/articles/PMC3074457/)[https://www.ncbi.nlm.nih.gov/pmc/articles/PMC3074457/](https://www.ncbi.nlm.nih.gov/pmc/articles/PMC3074457/?report=abstract%20https://www.ncbi.nlm.nih.gov/pmc/articles/PMC3074457/).
- [73] S. M. Smith, "Fast robust automated brain extraction," *Human brain mapping*, vol. 17, pp. 143–155, 3 Nov. 2002, issn: 1065-9471. doi: [10.1002/HBM.10062](https://doi.org/10.1002/HBM.10062). [Online]. Available: <https://pubmed.ncbi.nlm.nih.gov/12391568/>.
- [74] Y. Hirano, B. Stefanovic, and A. C. Silva, "Spatiotemporal evolution of the functional magnetic resonance imaging response to ultrashort stimuli," *Journal of Neuroscience*, vol. 31, pp. 1440–1447, 4 Jan. 2011, issn: 0270-6474. doi: [10.1523/JNEUROSCI.3986-10.2011](https://doi.org/10.1523/JNEUROSCI.3986-10.2011). [Online]. Available: <https://www.jneurosci.org/content/31/4/1440><https://www.jneurosci.org/content/31/4/1440.abstract>.
- [75] J. Martindale, J. Mayhew, J. Berwick, *et al.*, "The hemodynamic impulse response to a single neural event," *Journal of Cerebral Blood Flow and Metabolism*, vol. 23, pp. 546–555, 5 May 2003, issn: 0271678X. doi: [10.1097/01.WCB.0000058871.46954.2B/ASSET/IMAGES/LARGE/10.1097_01.WCB.0000058871.46954.2B-FIG9.JPEG](https://doi.org/10.1097/01.WCB.0000058871.46954.2B/ASSET/IMAGES/LARGE/10.1097_01.WCB.0000058871.46954.2B-FIG9.JPEG). [Online]. Available: <https://journals.sagepub.com/doi/10.1097/01.WCB.0000058871.46954.2B>.
- [76] *Chapter 3: The hemodynamic response function (hrf) — andy's brain book 1.0 documentation*. [Online]. Available: https://andysbrainbook.readthedocs.io/en/latest/fMRI_Short_Course/Statistics/03_Stats_HRF_Overview.html.
- [77] M. F. Glasser, S. N. Sotiropoulos, J. A. Wilson, *et al.*, "The minimal preprocessing pipelines for the human connectome project," *NeuroImage*, vol. 80, p. 105, Oct. 2013, issn: 10538119. doi: [10.1016/J.NEUROIMAGE.2013.04.127](https://doi.org/10.1016/J.NEUROIMAGE.2013.04.127). [Online]. Available: [/pmc/articles/PMC3720813/](https://www.ncbi.nlm.nih.gov/pmc/articles/PMC3720813/)[https://www.ncbi.nlm.nih.gov/pmc/articles/PMC3720813/](https://www.ncbi.nlm.nih.gov/pmc/articles/PMC3720813/?report=abstract%20https://www.ncbi.nlm.nih.gov/pmc/articles/PMC3720813/).

- [78] *Connectomedb*. [Online]. Available: <https://db.humanconnectome.org/app/template/Login.vm>.
- [79] M. Jenkinson, C. F. Beckmann, T. E. Behrens, M. W. Woolrich, and S. M. Smith, "Fsl," *NeuroImage*, vol. 62, pp. 782–790, 2 Aug. 2012, issn: 1053-8119. doi: 10.1016/J.NEUROIMAGE.2011.09.015. [Online]. Available: <https://linkinghub.elsevier.com/retrieve/pii/S1053811911010603>.
- [80] *Neurosynth: (0, 0, 0)*. [Online]. Available: <https://neurosynth.org/locations/>.
- [81] *Cosmo independent samples partitioner — cosmo multivariate pattern analysis toolbox 1.0rc1 documentation*. [Online]. Available: https://www.cosmomvpa.org/matlab/cosmo_independent_samples_partitioner.html#cosmo-independent-samples-partitioner.
- [82] *Different types of machine learning models*. [Online]. Available: <https://www.enjoyalgorithms.com/blog/classification-of-machine-learning-models>.
- [83] *Cosmo classify libsvm — cosmo multivariate pattern analysis toolbox 1.0rc1 documentation*. [Online]. Available: https://www.cosmomvpa.org/matlab/cosmo_classify_libsvm.html#cosmo-classify-libsvm.
- [84] C. Cortes and V. Vapnik, "Support-vector networks," *Machine Learning 1995 20:3*, vol. 20, pp. 273–297, 3 Sep. 1995, issn: 1573-0565. doi: 10.1007/BF00994018. [Online]. Available: <https://link.springer.com/article/10.1007/BF00994018>.